Variable C/P composition of organic production and its effect on ocean carbon storage in glacial model simulations

Malin Ödalen[1], Jonas Nycander[1], Andy Ridgwell[2,3], Kevin I. C. Oliver[4], Carlye D. Peterson[2], and Johan Nilsson[1]

[1]Department of Meteorology, Bolin Centre for Climate Research, Stockholm University, 106 91 Stockholm, Sweden
[2]Department of Earth Sciences, University of California–Riverside, Riverside, CA 92521, USA
[3]School of Geographical Sciences, Bristol University, Bristol BS8 1SS, UK
[4]National Oceanography Centre, Southampton, University of Southampton, Southampton SO14 3ZH, United Kingdom

Correspondence: Malin Ödalen (malin.odalen@misu.su.se)

Abstract. During the four most recent glacial maxima, atmospheric CO_2 has been lowered by about 90–100 ppm with respect to interglacial concentrations. It is likely that most of the atmospheric CO_2 deficit was stored in the ocean. Changes of the biological pump, which are related to the efficiency of the biological carbon uptake in the surface ocean and/or of the export of organic carbon to the deep ocean, have been proposed as a key mechanism for the increased glacial oceanic CO_2 storage.

5 The biological pump is strongly constrained by the amount of available surface nutrients. In models, it is generally assumed that the ratio between elemental nutrients, e.g. phosphorus, and carbon (C/P ratio) in organic material is fixed according to the classical Redfield ratio. The constant Redfield ratio appears to hold approximately when averaged over basin scales, but observations document highly variable C/P ratios on regional scales and between species. If the C/P ratio decreases when nutrient availability is scarce, as observations suggest, this has the potential to further increase glacial oceanic CO_2 storage

10 in response to changes in surface nutrient distributions. In the present study, we perform a sensitivity study to test how a phosphate–concentration dependent C/P ratio influences the oceanic CO_2 storage in an Earth system model of intermediate complexity (cGENIE). We carry out simulations of glacial–like changes in albedo, radiative forcing, wind–forced circulation, remineralisation depth of organic matter, and mineral dust deposition. Specifically, we compare model versions with with the classical constant Redfield ratio and an observationally–motivated variable C/P ratio, in which the carbon uptake increases with

15 decreasing phosphate concentration. While a flexible C/P ratio does not impact the model's ability to simulate benthic $\delta^{13}C$ patterns seen in observational data, our results indicate that, in production of organic matter, flexible C/P can further increase the oceanic storage of CO_2 in glacial model simulations. Past and future changes in the C/P ratio thus have implications for correctly projecting changes in oceanic carbon storage in glacial–to–interglacial transitions as well as in the present context of increasing atmospheric CO_2 concentrations.

20 ## 1 Introduction

During the last four glacial maxima, atmospheric CO_2 (henceforth pCO_2^{atm} was lowered by $\sim$ 90–100 ppm compared to the interglacials (e.g., Petit et al., 1999). Due to the difference in size between the oceanic, terrestrial and atmospheric carbon

reservoirs, where the oceanic reservoir is by far the largest with >90% of their summed carbon contents (e.g., Ciais et al., 2013), it is likely that most of the CO_2 that was removed from the atmosphere was stored in the glacial ocean.

Numerous processes have been identified as possible contributers to increased glacial oceanic storage, for example changes in the strength of the biological pump (e.g., Sarmiento and Toggweiler, 1984; Martin, 1990; Archer et al., 2000; Sigman

5 and Boyle, 2000), sedimentary processes (Broecker, 1982a, e.g.,), changes in ocean circulation and sea ice cover (e.g., Boyle and Keigwin, 1987; Duplessy et al., 1988; Stephens and Keeling, 2000; Menviel et al., 2017). Extensive summaries of these processes, and examples of their interactions, are given by e.g. Brovkin et al. (2007); Kohfeld and Ridgwell (2009); Hain et al. (2010); Sigman et al. (2010). Despite the efforts of identifying the responsible processes, models have been struggling to achieve the full lowering of pCO_2^{atm} expected for a glacial.

10 In this paper, we focus on the biological pump and how it responds to glacial–like changes in climate. Our aim is to investigate how the level of simplification of the biological carbon uptake in an Earth system model model may affect the glacial drawdown of pCO_2^{atm}. Most biogeochemical models used in glacial climate studies have a simple representation of biological production, which assumes that carbon, C, and inorganic nutrients such as phosphorus, P, are taken up in fixed proportion to each other. This is modelled using the average ratio of C/P of the ocean organic matter originally observed by Redfield (1963)

15 (C/P = 106/1), or adjustments to these suggested by e.g. Takahashi et al. (1985) and Anderson and Sarmiento (1994).

We investigate whether allowing for a flexible C/P stoichiometric ratio increases model ocean CO_2 storage in a glacial–like climate. This possibility was suggested by e.g. Broecker (1982b), Archer et al. (2000) and Galbraith and Martiny (2015), but the implications of Redfield versus flexible C/P for glacial ocean carbon storage has not previously been tested in an Earth system model. This type of non–Redfieldian dynamics were applied in the model used in Eggleston and Galbraith (2018) and

20 Galbraith and de Lavergne (2018), but their results were not analysed in terms of difference from a Redfield model version.

We conduct a sensitivity study, where we make glacial–like changes in radiative forcing, albedo, wind–forced circulation, remineralisation depth and dust, separately and in combination. We apply these perturbations in two different versions of the Earth system model cGENIE; an original version using fixed Redfield stoichiometry of C/P (Ridgwell et al., 2007) plus a co–limitation by iron (Tagliabue et al., 2016) for biological production, and a modified version using the non–Redfieldian, nutrient

25 concentration dependent, C/P stoichiometry suggested by Galbraith and Martiny (2015) and iron co–limitation.

We show that flexible C/P stoichiometry allows a larger glacial ocean CO_2 storage, as predicted by the box–model study of Galbraith and Martiny (2015), and that flexible stoichiometry has the largest impact for perturbations in remineralisation depth and dust forcing. Additionally, we show that flexible stoichiometry allows for increased ocean carbon storage without decreasing the storage of preformed nutrients in the deep ocean.

30 ## 2 Methods

2.1 Model description

cGENIE is an Earth system model of intermediate complexity, with a 3D frictional–geostrophic ocean (36×36 equal area horizontal grid, 16 depth levels), 2D energy–moisture balance atmosphere with prescribed wind fields, interactive atmospheric

chemistry and ocean biogeochemistry. Model code and user handbook can be found in the cGENIE GitHub repository (cGENIE GitHub repository, 2019). We run a version of cGENIE with the same phosphorus plus iron (Fe) co–limitation scheme as used in the iron cycle model inter–comparison study of Tagliabue et al. (2016). The model branch enabled for use with flexible C:P ratios (see 2.2) is tagged as release v0.9.5, and the model configurations used in this paper are included in this release

5 (cGENIE release v0.9.5, 2019, see Code availability for details).

2.2 Stoichiometry

In the original version of the cGENIE Earth system model (Ridgwell et al., 2007), as well as in the version of Tagliabue et al. (2016), the stoichiometric ratios are based on Redfield (1963). Thus, there is a fixed relationship between the number of moles of the elements that are taken up (positive) or released (negative) during production of organic matter in the ocean. This

10 relationship is $P : C : O_2 = 1 : 106 : -138$, where O_2 is dissolved oxygen (nitrogen is assumed only implicitly for the purpose of accounting for organic matter creation and remineralisation related alkalinity transformations in the ocean (Ridgwell et al., 2007)). An exception is iron, where Fe:C varies as a function of iron availability as described in Watson et al. (2000).

Although the average elemental composition of organic matter in the ocean is close to the Redfield ratios, the stoichiometry of production of new organic material has shown high in–situ variability. Variability occurs between species, but also within

15 the same species, and has been shown to depend on environmental factors such as nutrient availability, water temperature and light (e.g., Le Quéré et al., 2005b; Galbraith and Martiny, 2015; Yvon-Durocher et al., 2015; Tanioka and Matsumoto, 2017; Moreno et al., 2018). We test the importance of this variability for glacial ocean CO_2 storage by running the same experiments with the fixed Redfield stoichiometry version of cGENIE and with a model version where we have implemented the linear regression model presented by Galbraith and Martiny (2015) (Eq. 1). These two model versions are henceforth denoted RED

20 and GAM, respectively.

The flexible stoichiometry in GAM depends on the ambient concentration of dissolved phosphate ($[PO_4]$) in the water:

$$P : C = 1 : (\frac{[PO_4]}{144.9 \mu mol L^{-1}} + 0.0060)^{-1}. \tag{1}$$

This relation shows that, when $[PO_4]$ is low, organisms bind more C per atom of P than they do under high $[PO_4]$ conditions (Fig. 1). Eq. 1 is applied in cGENIE in the calculations of biological C uptake at the surface ocean based on the surface

25 concentration of PO_4. In Section 3.1.2, Eq. 1 is also used to translate model surface PO_4 fields to the corresponding surface C/P ratios for the organic matter produced in each grid cell.

2.3 Experiments

We start all experiments from an interglacial/modern control state, which has been run for 10,000 years to steady state, using either Redfield ($Ctrl_{RED}$) or variable ($Ctrl_{GAM}$) stoichiometry. The control states have a prescribed pCO_2^{atm} of 278 ppm

30 and the same climate (Table 1), but due to the differences in C/P, they have different ocean carbon inventories (Table S.1.). In $Ctrl_{GAM}$, the export flux of organic matter (see Ridgwell et al., 2007) has a global average C/P composition of 121/1 and

thus the global ocean carbon storage is larger than in $Ctrl_{RED}$. This also suggest that a perturbation, which increases ocean storage of P through the biological pump, could cause storage of 15 (i.e. 121-106) more carbon atoms in simulations using GAM compared to RED, simply because the average composition of the formed biological material is different. To distinguish between the role of the flexibility of the stoichiometry and the change in the mean composition of organic material, we add a

5   control state with fixed stoichiometry where C/P = 121/1 (henceforth denoted $Ctrl_{121}$).

In order to explore the effects of variable stoichiometry, we make a sensitivity study where we apply changes to boundary conditions, individually and in combination (see Section 2.3.3), that may be representative of changes that occurred during glacial periods. All experiments are listed in Table 1.

The applied changes in boundary conditions are

10   – physical perturbations (colder climate):

      – radiative forcing corresponding to LGM CO$_2$ = 185 ppm

      – zonal albedo profile representative of LGM (calculated from the LGM climate simulation of Davies-Barnard et al., 2017)

  – physical perturbations (weaker overturning):

15   – reduced wind forcing over the Southern Ocean (Lauderdale et al., 2013, e.g.,) and north of 35°N (see Section 2.3.1).

  – biological perturbations:

      – changed remineralisation length scale (e.g., Matsumoto, 2007; Chikamoto et al., 2012; Menviel et al., 2012)

      – increased dust forcing, as simulated for LGM (regridded from Mahowald et al., 2006)

By applying the above perturbations, we aim to achieve some of the characteristics of the Last Glacial Maximum (LGM)

20   ocean, which appears to have had a global average ocean temperature ($\overline{T_{oce}}$) 2.7°C colder than the Holocene (Headly and Severinghaus, 2007), a weakly ventilated deep ocean (e.g., Menviel et al., 2017) and a more efficient biological pump (e.g., Sarmiento and Toggweiler, 1984; Martin, 1990; Sigman and Boyle, 2000). We also aim to increase carbon retention in the deep ocean (Muglia et al., 2018).

The physical perturbations serve to achieve a colder climate (e.g., $\overline{T_{oce}}$, cools by 2.1°C c.f. $Ctrl$, thus nearly 80 % of

25   the observed 2.7°C, see Section3.2.1) and weaker overturning (see Section 3.2.2 and Fig. 2) with a longer residence time of the Antarctic Bottom Water (AABW) cell compared to $Ctrl$. Colder conditions achieve a stronger solubility pump, thereby strengthening the retention of carbon in the deep ocean. As the physical perturbations affect the ocean circulation and temperature, they thereby affect biological productivity, e.g. through changed rates in nutrient upwelling and slower growth in colder water (Ridgwell et al., 2007).

30   The biological perturbations serve to achieve a more efficient biological pump, which is connected with increased retention of nutrients and carbon in the deep ocean, and lower surface nutrient concentrations in productive regions (see Sections 3.2.3

and 3.2.4). With flexible stoichiometry, lower surface nutrient concentrations results in a higher C/P ratio, further increasing the export production, and therby the carbon retention in the deep ocean. In our experiments, we show that the flexible stoichiometry amplifies the response of the biological pump to both physical and biological perturbations.

The perturbations and the experiments are described in detail in Sections 2.3.1–2.3.3.

2.3.1 Physical perturbations

We change the physical conditions for climate by changing radiative forcing and albedo to LGM–like conditions and denote these changes $LGMphy$. We set the radiative forcing in the model to correspond to an atmosphere with 185 ppm CO_2 instead of 278. However, we allow the pCO_2^{atm} to freely evolve (starting from the value of 278 ppm of the $Ctrl$ state atmosphere) in response to the cooler climate. For albedo, we apply a zonal LGM albedo profile (calculated from the LGM climate simulation of Davies-Barnard et al., 2017). Assumptions of a simple zonal profile instead of e.g. a 2D field re–gridded from PMIP LGM simulations allows for a better consistency with the original zonal mean albedo profile developed for the modern configuration of GENIE (Marsh et al., 2011). Together, the changes in radiative forcing and albedo causes the global ocean average temperature ($\overline{T_{oce}}$) to decrease by 2.1°C compared to $Ctrl$ (see Section3.2.1).

To achieve a longer residence time of the AABW water mass, and an associated increase in carbon and nutrient retention, we apply weaker winds (denoted $WNA \times 0.5$). We use the Southern Ocean wind profile of Lauderdale et al. (2013), where the peak westerly wind strength at 50°S has been reduced half compared to the control state (see Section 2.3.3). The winds north and south of the peak are reduced accordingly to give a continuous profile (see Fig. 2 a of Lauderdale et al., 2013). The result is a weaker overturning (see Table 2) and a longer residence time of the AABW (see Section 4.5) as is expected for the glacial ocean (e.g., Menviel et al., 2017). Thus, this approach is justifiable in a model of reduced complexity. However, there are studies suggesting that the Southern Ocean winds may in fact have been stronger during glacial times(Sime et al., 2013; Kohfeld et al., 2013; Sime et al., 2016). To avoid an expansion of the NADW overturning cell that would be inconsistent with the glacial ocean (e.g., Curry and Oppo, 2005), winds north of 35°N are also gradually reduced so that the wind strength north of 50°N is reduced by half compared to the control state.

2.3.2 Biological perturbations

It has been hypothesised that the cooling of the glacial ocean led to a deepening of the remineralisation length scale (henceforth denoted RLS) in the ocean, and thereby more efficient retention of organic carbon in the deep ocean (e.g., Matsumoto, 2007; Chikamoto et al., 2012), which in turn caused a lowering of pCO_2^{atm}. However, Menviel et al. (2012) find that such a deepening results in model changes in export production (i.e. the amount of C captured by primary production that leaves the surface ocean without being remineralised) in poor agreement with paleo–proxies. Deeper remineralisation also results in increased nutrient retention in the deep ocean, thus causing changes in surface nutrient fields and in C/P ratios of GAM. We test the effect of changes in RLS by multiplying the model default RLS by a factor Y ($RLS \times Y$,see Section 2.3.3).

Increased dust forcing leads to increased iron (Fe) availability. This allows for increased productivity (and hence more efficient usage of other nutrients) in the high-nutrient, low-chlorophyll (HNLC) regions in the North Pacific, Equatorial Pacific

and Southern Ocean, where iron (Fe) is the limiting micronutrient (e.g., Martin, 1990). The variable stoichiometry in GAM is expected to be influential if the concentrations of P decrease in such regions as a result of increased Fe availability. This process may hence be of importance in a glacial scenario where dust forcing increases as a result of the drier conditions (e.g., Martin, 1990). We apply the regridded LGM dust fields of Mahowald et al. (2006) and denote this change $LGMdust$.

5   ### 2.3.3   Sensitivity experiments and combined simulations

In the sensitivity study, for each of the three C/P parametrisations, we first change one forcing at a time (see Table 1). We run simulations where we apply individually the LGM boundary conditions for radiative forcing ($LGMrf$), albedo ($LGMalb$) and dust ($LGMdust$) and one simulation with halved wind stress near the poles (-50 and 50°N) ($WNS \times 0.5$). For the remineralisation length scale (RLS), we test a range of values of the multiplication factor $RLS \times fr$, where $fr = \{0.75, 1.25, 1.75\}$.

10   This allows us to test the sensitivity to deep ocean retention of organic carbon.

We then run simulations where we combine several changes in forcing. We get a colder climate simulation ($LGMphy$) by combining $LGMrf$ and $LGMalb$. In simulation $Acomb$, we combine $LGMrf$, $LGMalb$, $LGMdust$, and $RLS \times 1.25$ (see Table 1). Kwon et al. (2009) show that small changes in remineralisation depth can cause substantial changes in pCO_2^{atm}. With the RLS deepening of 25%, we keep the corresponding changes in pCO_2^{atm} from exceeding the $\sim 20-30$ ppm obtained

15   in other studies (Matsumoto, 2007; Menviel et al., 2012). We finally run a glacial–like simulation $GLcomb$ (see Section 3.3), which is similar to $Acomb$ but also includes the change in wind stress $WSN \times 0.5$. The achieved $GLcomb$ model state has a colder climate (see Table **??**), reduced deep ocean ventilation and more carbon retention in the deep ocean compared to the control state.

2.4   Observations

20   For comparison and validation of model results, we use records of ocean state variables from observations of modern data and proxy data from the LGM.

Modern data of ocean temperature, oxygen and nutrients are retrieved from the World Ocean Atlas 2013 (Locarnini et al., 2013; Garcia et al., 2014b, a) and we use the proxy estimates of LGM ocean temperature from Headly and Severinghaus (2007). Average modern day strength of the Atlantic meridional overturning circulation (AMOC) is estimated by McCarthy

25   et al. (2015) from the RAPID-MOCHA array at 26 °N.

We use model–data comparison of benthic $\delta^{13}C$ to assess the statistical similarity (correlation) between both the model control state and glacial–like state (see Section 2.3) to benthic $\delta^{13}C$ data representing the Late Holocene (0-6 ka, HOL) and Last Glacial Maximum (19-23 ka, LGM), respectively Peterson et al. (2014). Locations of core sites can be seen in Fig. S.1. (see also Fig. 1 in Peterson et al. (2014)). Note that LGM benthic $\delta^{13}C$ is more ^{13}C-depleted than the Holocene due to the addition

30   of ^{13}C-depleted terrestrial carbon to the glacial ocean (Shackleton, 1977; Curry et al., 1988; Duplessy et al., 1988), which is not simulated in our model experiments. Therefore, to compare our glacial–like simulations ($GLcomb$) to LGM observations, we subtract a Holocene-LGM global average difference of 0.32 ‰ (Gebbie et al., 2015) from the $GLcomb$ experiments. Gebbie et al. (2015) state that the wide range of error for the estimate of glacial–to–modern change in benthic $\delta^{13}C$ of of 0.32 ± 0.20‰

suffers from a lack of observations in all ocean basins but the Atlantic. Therefore, we place more emphasis on the results of the model–data comparison in the Atlantic than in the Indo–Pacific sector.

2.5 Nutrient utilisation efficiency

The extent to which biology succeeds to use the available nutrients can be determined by calculating the nutrient utilisation efficiency $\overline{P^*}$ (Ito and Follows, 2005; Ödalen et al., 2018),

$$\overline{P^*} = \frac{\overline{P_{rem}}}{\overline{P_{tot}}}, \tag{2}$$

which is the fraction of remineralised (P_{reg}) to total (P_{tot}) nutrients (in this case, PO$_4$) in the ocean. Overlines denote global averages. Remineralised nutrients have been transported from the surface to the interior ocean by the biological pump, and P_{rem} is given by

$$P_{rem} = P_{tot} - P_{pre}. \tag{3}$$

Here, P_{pre} is preformed PO_4 – the concentration of PO_4 that was present in the water parcel as it sank, thus the fraction that was not used by biology in the surface ocean. In cGENIE, the concentration of preformed tracers is set in the surface ocean and then passively advected through the ocean interior (**?**). The biological pump also captures carbon, and a similar relationship can be used for concentrations of DIC, where

$$DIC_{rem} = DIC_{tot} - DIC_{pre}. \tag{4}$$

DIC_{rem} is used to compute the ocean storage of remineralised acidic carbon (AC_{rem}, see Appendix A). AC_{rem} is biological carbon that entered the ocean in the form of CO$_2$ in soft tissue (as opposed to carbonates in hard tissue), measured independent of oxygen consumption and/or remineralised phosphate.

In cGENIE, P_{pre} and DIC_{pre} are modelled as passive tracers (Ödalen et al. (2018)). Hence, we can use the model output for P_{pre} in Eq. 3 to compute $\overline{P^*}$ (Eq. 2).

In a model with fixed Redfield ratio, $\overline{P^*}$ determines the effect of the biological pump on pCO_2^{atm}. For example, it has been found that a higher $\overline{P^*}$ in the initial state gives a lower potential for drawdown of pCO_2^{atm} in response to similar perturbations (Marinov et al., 2008; Ödalen et al., 2018). However, with variable stoichiometry this is no longer true, since the amount of carbon retained in the deep ocean is not necessarily proportional to $\overline{P^*}$.

Biogeosciences
Discussions

3 Results

3.1 Control states

3.1.1 Ocean temperature and circulation

As the three control states, $Ctrl_{RED}$, $Ctrl_{GAM}$ and $Ctrl_{121}$ are driven by the same physical forcings and have the same

5   pCO_2^{atm}, they have the same ocean circulation pattern (Fig. 2 a, c, e and Table 2, Table S.2.) and climate (exemplified by global ocean average temperature ($\overline{T_{oce}}$) in Table 2 and Table S.2.). The surface ocean nutrient fields are fairly similar, with small differences due to the different C/P parametrisations (compare Fig. 3 a, and Fig. S.2.). The strength of the Atlantic meridional overturning circulation (AMOC), diagnosed in the model as the maximum of the Atlantic meridional overturning streamfunction deeper than 1000 m, is 14 SV ($1 SV = 1 \cdot 10^6 m^3 s^{-1}$) in all control states (Table 2, Table S.2.).Results from the

10   RAPID-MOCHA array at 26 °N suggest an average AMOC strength of 17.2 ± 0.9 SV (McCarthy et al., 2015), thus our control state AMOC is a little bit weaker than in present day climate. The observational estimate for $\overline{T_{oce}}$ according to the World Ocean Atlas 2013 (Locarnini et al., 2013) is 3.49 °C, thus comparable to the 3.56 °C of our $Ctrl$ simulations. The surface nutrient concentrations of our control state $Ctrl_{GAM}$ (Fig. 3 a) compare reasonably well with observed surface ocean concentrations of PO$_4$ (Fig. 3 c), with some underestimation in the the Pacific equatorial region, the North Pacific ocean, and the Labrador

15   Sea. The agreement with observations is better for $Ctrl_{GAM}$ than for $Ctrl_{RED}$ (Fig. S.2.).

3.1.2 Surface nutrient distribution and C/P ratios

In Fig. 3 we see that surface PO_4 fields (left hand column) and the corresponding fields of surface C/P ratios (as given by Eq. 1, right hand column) of $Ctrl_{GAM}$ (panels a, b) and of observations (panels c, d) are similar in their pattern as well as in the magnitudes of values. Note that high concentrations of PO$_4$ correspond to low C/P ratios, and vice versa. The highest

20   observed PO_4 concentrations in the Northern and equatorial Pacific are not fully reproduced by the model, but the pattern is well reproduced. In the surface C/P field of $Ctrl_{GAM}$ (Fig. 3 b) we see the signature of very high nutrient concentrations in the Southern Ocean ($> 1 \mu mol L^{-1}$, Fig. 3 b) as a band of low ratios, with the most extreme values near the Antarctic continent, as seen in observations (Fig. 3 d).

The nutrient utilisation efficiency $\overline{P^*}$(Eq. 2) in the three control states differs by a few percent; 0.43, 0.46 and 0.42 in

25   $Ctrl_{RED}$, $Ctrl_{GAM}$ and $Ctrl_{121}$ respectively (Table 2). The fraction of DIC_{rem} in DIC_{tot} (see Section 2.5, Eq. 4, Table S.1.) is 0.065, 0.077 and 0.072 in $Ctrl_{RED}$, $Ctrl_{GAM}$ and $Ctrl_{121}$ respectively.

3.1.3 Ocean dissolved O_2

The most apparent difference between $Ctrl_{RED}$ and $Ctrl_{GAM}$ is in deep ocean oxygen concentrations, where the global ocean average dissolved O_2 concentration ($\overline{O_2}$) in $Ctrl_{GAM}$ ($144 \mu mol kg^{-1}$) is lower than in $Ctrl_{RED}$ and $Ctrl_{121}$ (166 and

30   $171 \mu mol kg^{-1}$, respectively). Compared to observations (World Ocean Atlas 2013, Fig. 4 a–b), both $Ctrl_{RED}$ (Fig. 4 c–d) and $Ctrl_{GAM}$ (Fig. 4 e–f) agree reasonably well with the real ocean. $Ctrl_{GAM}$ appears to capture better than $Ctrl_{RED}$ the

equatorial oxygen minimum in the Atlantic basin, but goes too low in the North Pacific. In $Ctrl_{GAM}$ (Fig. 4 f), the North Pacific is markedly lower in oxygen than in $Ctrl_{RED}$ (Fig. 4 d) and even anoxic in the oxygen minimum zone (OMZ). This should be kept in mind when analysing the oxygen sections of the glacial–like states $GLcomb_{RED}$ (Fig. 4 g–h) and $GLcomb_{GAM}$ (Fig. 4 i–j). Global averages for dissolved O_2 are given in Table 2.

5 ### 3.1.4   Ocean $\delta^{13}C$

By comparing $Ctrl_{RED}$ $\delta^{13}C$ and Holocene (0–6 ka, HOL) benthic $\delta^{13}C$ values, we estimate a global model–data correlation of 0.78 (Table S.3.). The modern–day Atlantic Ocean has a distinctive spatial $\delta^{13}C$ pattern (Fig. 5 a, Fig. S.1.) with ^{13}C-enriched values in the intermediate depth (<2 km) North Atlantic and Nordic Seas and ^{13}C-depleted values in the deep (>2.5 km) South Atlantic. While the model produces a weaker gradient than the observed HOL Atlantic Ocean (corr. 0.50, Table

10 S.3.) the model correlates well with Eastern Atlantic $\delta^{13}C$ records (Fig. S.1.). For the Indo–Pacific, the weaker benthic $\delta^{13}C$ gradient is well represented by the model (Fig. 5 e). This pattern emerges mainly due to ^{13}C-depleted, biologically sourced carbon that is accumulated in the weak circulation region of the interior North Pacific (e.g., Matsumoto et al., 2002). However, Indo–Pacific $\delta^{13}C$ values of $Ctrl_{RED}$ are overall lower than the HOL observations. The overall model–data correlation for the Indo–Pacific is 0.39 (Table S.3.). Comparing the control states of the RED and GAM model versions, $\delta^{13}C$ patterns (Fig. 5 a,

15 e and Fig. S.3. a, e) and model–data correlations with HOL observations (Table S.3.) are similar between the model versions, with somewhat lower correlations for GAM.

3.2   Sensitivity experiments

The applied changes listed in Table 1 cause changes in e.g. ocean overturning, temperature, surface nutrient distributions and biological productivity, which result in changed pCO_2^{atm}. The resulting steady state global average values for temperature

20 ($\overline{T_{oce}}$), dissolved oxygen ($\overline{O_2}$), and nutrient utilisation efficiency $\overline{P^*}$, as well as the maximum and minimum of the Atlantic meridional overturning streamfunction, are listed in Table 2.

3.2.1   Radiative forcing and albedo

In the simulations where radiative forcing and albedo are changed to represent LGM conditions ($LGMrf + LGMalb = LGMphy$), the reductions in pCO_2^{atm} are similar in the RED and the GAM model versions. In $LGMphy$, the resulting

25 pCO_2^{atm} is 245.4 and 244.9 ppm respectively, thus a reduction of 33 ppm compared to the $Ctrl$ 278 ppm (Fig. 6). Here, variable C/P does not impact the results, because changes in the surface nutrient distribution (Fig. 7 a), and the associated changes in C/P (Fig. 8 a), are limited to very high latitudes where productivity is already low in the control state, due to low temperatures and a lack of light and iron. The drawdown of pCO_2^{atm} can mainly be attributed to the increase in solubility carbon ($C_{sat,T}$) due to ocean cooling, and to an increase in sea ice, which prevents air–sea gas exchange and therefore causes

30 an increase in disequilibrium carbon (C_{dis}) (Ödalen et al., 2018). Ocean cooling amounts to 2.1°C in $LGMphy$ compared to $Ctrl$ ($\overline{T_{oce}}$ in Table 2). In cGENIE, the increase in $C_{sat,T}$ associated with ocean cooling corresponds to $\sim 7 \pm 1.5$ ppm $°C^{-1}$

Biogeosciences
Discussions

(Ödalen et al., 2018, supplementary Fig. S.1.). Thus, in $LGMphy$ $C_{sat,T}$ and C_{dis} should contribute roughly 40 and 60 % respectively of the change in pCO_2^{atm}. Note that cGENIE underestimates the true effect of ocean cooling on solubility, due to a temperature restriction on the solubility constants (Ödalen et al., 2018). This temperature restriction limits solubility from changing below 2.0 °C. In this case, the solubility effect on pCO_2^{atm} of reducing $\overline{T_{oce}}$ by 2.1 °C (from 3.6 °C to 1.5°C, ~ 15

5   ppm) is thus comparable to only 1.6 °C of cooling (from 3.6 °C to 2.0 °C, ~ 11 ppm), and the solubility effect is underestimated by ~ 4 ppm.

3.2.2 Reduced wind forcing

When the peak of Southern Ocean (henceforth SO) winds is reduced, the strength of the overturning circulation of AABW decreases (see difference in Southern Hemisphere overturning streamfunction between Fig. 2 a and b). Thus, given that the

10   volume of AABW does not change, its residence time increases. This also means that the upwelling nutrient–rich water in the SO stays a longer time near the surface and loses more nutrients before being subducted. This decreases the SO concentration of preformed phosphate in $WNS \times 0.5_{RED}$ compared to $Ctrl$, as seen in Fig. 7 b, and increases the nutrient utilisation efficiency $\overline{P^*}$ (Table 2, Fig. 9). This leads to a drawdown of pCO_2^{atm} of 12.9 ppm compared to $Ctrl_{RED}$ (Fig. 6). As the nutrient concentration in the SO decreases (Fig. 7 b), the flexible C/P ratio (Fig. 8 b) leads to an increased carbon capture efficiency in

15   GAM compared to RED (see $GLcomb-Ctrl$ of biologically sourced carbon (AC_{rem}) in Fig. 9), which is partly compensated by a reverse effect in the Pacific equatorial region. Consequently, in $WSN \times 0.5_{GAM}$, we get a reduction of pCO_2^{atm} of 16.3 ppm compared to $Ctrl_{GAM}$ (Fig. 6). Hence, for halved peak wind stress at ± 50°N, the flexible stoichiometry increases the drawdown by ~ 26 %. In a simulation with reduced wind stress and fixed C/P stoichiometry of 121/1 ($WNS \times 0.5_{121}$, we get a pCO_2^{atm} of 263.5 ppm, thus a drawdown of 14.5 ppm. This indicates that, in this case, about half of the effect of the variable

20   stoichiometry can be attributed to a difference in the mean C/P composition of the organic material between the control states $Ctrl_{RED}$ and $Ctrl_{GAM}$.

3.2.3 Remineralisation length scale

When the remineralisation length scale (RLS) increases, the biological material reaches deeper before it is remineralised, and it takes longer for it to be returned to the surface. Therefore, more of the biologically sourced carbon (AC_{rem}) and nutrients

25   are present in the deep ocean at any given time, leading to an increase in $\overline{P^*}$ (Table 2, Fig. 9) and a decrease in pCO_2^{atm} (Fig. 6). The deeper we make the RLS, the bigger the drawdown of pCO_2^{atm} – in $RLS \times 1.25_{RED}$ and $RLS \times 1.75_{RED}$ pCO_2^{atm} decreases by 14 and 33 ppm, respectively, compared to $Ctrl_{RED}$. In GAM, the drawdown in each experiment is increased by an additional ~ 30 %, thus $RLS \times 1.25_{GAM}$ and $RLS \times 1.75_{GAM}$ see a reduction of pCO_2^{atm} of 18 and 44 ppm, respectively, compared to $Ctrl_{GAM}$ (Table S.2.). Our changes in RLS cause very small, but global, changes in surface nutrients

30   (ex. $RLS \times 1.25$ in Fig. 7 c), which, through the small resulting changes in C/P (Fig. 8 c), still contribute to the additional drawdown of pCO_2^{atm} in GAM. Experiments with deeper RLS in 121 ($RLS \times 1.25_{121}$ and $RLS \times 1.75_{121}$), suggest that about 40 % of the observed pCO_2^{atm} differences can again be attributed to the difference in export flux average C/P in the control state.

In a sensitivity test where we make the RLS 25 % shallower (which would be representative of a warmer climate c.f. $Ctrl$), the pCO_2^{atm} increases by 18 and 23 ppm in RED and GAM respectively compared to their control states (see $RLS \times 0.75_{RED}$ and $RLS \times 0.75_{GAM}$ in Table S.2.). Interestingly, the response in pCO_2^{atm} is again ~ 30 % larger in GAM. The variable stoichiometry thus amplifies the effect on pCO_2^{atm} by any change in RLS.

3.2.4 Dust forcing

The simulations with LGM dust forcing ($LGMdust$, Table 1) show the largest difference in pCO_2^{atm} between the RED and the GAM. In $LGMdust_{RED}$, pCO_2^{atm} decreases by 16 ppm compared to $Ctrl_{RED}$, whereas $LGMdust_{GAM}$ sees a reduction of 21 ppm compared to $Ctrl_{GAM}$ (Fig. 6). The drawdown is thus ~ 30 % larger with variable stoichiometry. ~ 10 % can be explained by a change in average composition of the exported organic material (see $LGMdust_{121}$ in Table S.2., where the the drawdown is 18 ppm, and ~ 10 % larger than in $LGMdust_{RED}$).

As anticipated, the iron added by the dust forcing allows more efficient usage of P in the HNLC-regions, which increases $\overline{P*}$ and the ocean storage of biologically sourced carbon (Table 2, Fig. 9). This reduces the surface nutrient concentrations in these areas (Fig. 7 d). In the GAM model version, this is followed by increased C/P ratios in these areas (Fig. 8 d), resulting in a lower pCO_2^{atm} in $LGMdust_{GAM}$ than in $LGMdust_{RED}$. The largest anomalies in PO_4 concentrations, and consequently in C/P, are observed in subantarctic zone of the Southern Ocean, particularly in the Atlantic and Indian sectors. This subantarctic increase in biological efficiency is consistent with radionuclide proxy data from the LGM (e.g., Kumar et al., 1995; Kohfeld et al., 2005).

3.3 Combined experiments

We show the results of two different combined simulations; $Acomb$ and $GLcomb$. $GLcomb$ is the "glacial–like" simulation, which combines all the sensitivity experiments (Table 1). $Acomb$ omits the reduction in wind stress.

3.3.1 Ocean temperature and circulation

In the glacial–like simulations, $GLcomb_{RED}$ and $GLcomb_{GAM}$, the global average ocean temperature ($\overline{T_{oce}}$) is 1.7 °C lower than in the respective control states (Table 2). Headly and Severinghaus (2007) estimate LGM $\overline{T_{oce}}$ to have been 2.6 ± 0.6 °C colder than the modern ocean. $GLcomb$ is thus just outside the one standard deviation limit of the warm end of this estimate. In $Acomb$, $\overline{T_{oce}}$ is 2.1°C cooler than $Ctrl$, thus this simulation falls within the uncertainty of the Headly and Severinghaus (2007) estimate for the LGM.

Ocean overturning circulation weakens in $GLcomb$ compared to $Ctrl$ (Fig. 2, Table 2), mainly as a result of the wind stress reduction. For example, the AMOC (here measured as the maximum of the Atlantic overturning streamfunction) reduces in strength by ~ 15 %, from 14 Sv to 12 SV (Table 2). The global meridional overturning stream function reveals that the SO overturning cell sees a reduction in transport (Fig. 2 d), which is associated with weaker upwelling and thus longer residence

time for AABW, as hypothesised for the glacial ocean (e.g., Menviel et al., 2017). In $Acomb$, where the wind stress is kept at modern values, the ocean overturning circulation remains similar to the control state (Table 2).

3.3.2 Surface nutrient distribution and C/P ratios

In the surface nutrient anomalies ($GLcomb - Ctrl$, shown for GAM in Fig. 7 f), we see the strongest response in the Southern

5 Ocean, with different effects south and north of the so-called biogeochemical divide described by Marinov et al. (2006). Marinov et al. (2006) show that the air–sea balance of CO_2 is dominated by processes in the waters close to Antarctica, whereas global export production is instead controlled by the biological pump and circulation in the Subantarctic region. The border between these two regimes is referred to as the biogeochemical divide. South of the biogeochemical divide, close to the Antarctic continent, we see an increase in $GLcomb$ nutrient concentrations compared to $Ctrl$ (Fig. 7 f), which coincides with

10 an increase in sea-ice in this area (not shown). Colder conditions due to changed albedo and radiative forcing, with more sea ice than in the control state, cause a reduction in biological production, leaving more unused P in the surface layer (Fig. 7 a). North of the biogeochemical divide, increased aeolian dust flux increases the productivity of the biology, which reduces P in the surface compared to the control (Fig. 7 d). In combination with circulation changes, resulting from the reduced SO wind stress (Fig. 7 b), and deeper remineralisation (Fig. 7 c), P concentrations in the Subantarctic region are strongly reduced (Fig.

15 7 f). In the North and Equatorial Pacific, there is also a reduction of P (Fig. 7 f), mainly due to to the increased dust flux (Fig. 7 d). There is an increase in P seen in the Arctic, again coincident with an increase in sea ice in the same area. As a result of these changes, we see strong positive anomalies in C/P in the HNLC-regions, and negative anomalies in the highest latitude bands (Fig. 8 f). The organic matter that is exported out of the upper layer (henceforth referred to as export production) in $GLcomb_{GAM}$ has a global average C/P ratio of 134/1.

20 ### 3.3.3 Ocean dissolved O_2

Despite colder conditions, which allow for more dissolution of O_2, the reduction in $\overline{O_2}$ is evident in the $GLcomb$–simulations (Fig. 4). This mirrors the increase of AC_{rem} (Fig. 9). The $\overline{O_2}$ reduction is about 50 % larger in GAM compared to RED. As the initial state $Ctrl_{GAM}$ is already lower in oxygen than $Ctrl_{RED}$ ($144 \mu mol kg^{-1}$ compared to $166 \mu mol kg^{-1}$), and variable stoichiometry allows for additional ocean storage of organic carbon, the end state $\overline{O_2}$ is drastically lower in $GLcomb_{GAM}$

25 ($74 \mu mol kg^{-1}$) compared to $GLcomb_{RED}$ ($122 \mu mol kg^{-1}$) and $GLcomb_{121}$ ($124 \mu mol kg^{-1}$).

3.3.4 Ocean $\delta^{13}C$

In $GLcomb_{RED}$ (contours in Fig. 5 b,d), the Atlantic North–South gradient in $\delta^{13}C$ is stronger than in $Ctrl_{RED}$ (contours in Fig. 5 a,c). This strong gradient is not observed in the Holocene Atlantic $\delta^{13}C$-data (dots in Fig. 5 a,b), but is prominent in the LGM time slice (dots in Fig. 5 c,d). The LGM observations are well reproduced in $GLcomb_{red}$ (corr. 0.62, Table S.3.),

30 especially in the East Atlantic (corr. 0.77). When we correct $GLcomb_{RED}$ for the absence of injected terrestrial carbon, we see clear similarities with LGM observations (Fig. 5 d), though the southernmost cores still indicate more ^{13}C-depleted conditions

than the model. In the Indo–Pacific, $GLcomb_{RED}$ is too ^{13}C-depleted compared to LGM observations, particularly with the correction for the absence of a terrestrial signal (Fig. 5 h), and the model–data correlation is poor (0.05). For the Indo–Pacific, the model–data correlation for Holocene data is similar between $GLcomb_{RED}$ and $Ctrl_{RED}$ (0.24 and 0.39 respectively, Table S.3.). This suggests that the poor correlation with LGM data is simply due to our changes in forcings being insufficient

5   to achieve the required rearrangements in Indo–Pacific circulation patterns. In $GLcomb$, similarly as in $Ctrl$, there is very little difference between the RED and GAM model versions in terms of $\delta^{13}C$ patterns (compare Fig. 5 d,h to Fig. S.3. d,h) and model–data correlations (Table S.3.). However, there are overall lower values of $\delta^{13}C$ in GAM, reflecting the larger storage of biologically sourced carbon in the deep ocean in this model version.

3.3.5 Atmospheric CO_2

10   In the combined experiments $Acomb$ and $GLcomb$, pCO_2^{atm} decreases strongly compared to the control state (-56 to -80 ppm, Fig. 6). This is partly a result of colder conditions (Table 2), which lead to increased solubility for CO_2 in sea water, and also cause increased C_{dis}, because of expanded sea ice cover (not shown) which restricts air–sea gas exchange. This slows down the equilibration of the CO_2–rich upwelling water with the atmosphere before it is subducted into the deep ocean. Changes in biological production (see Section 3.3.2) and storage of biologically sourced carbon, Fig. 9, also contribute strongly to the

15   reduced pCO_2^{atm}. In $GLcomb_{RED}$ and $GLcomb_{GAM}$, we achieve drawdown of pCO_2^{atm} of 64 and 80 ppm, respectively, from the 278 ppm of the control states (Fig. 6). This corresponds to an increase in ocean carbon storage of 139 PgC and 173 PgC , respectively (Table S.1.). The drawdown is thus 25 % larger in GAM than in RED. If we compare this to $GLcomb_{121}$ (drawdown of 72 ppm, Fig. 6), we see that about half (8 ppm) of this can be attributed to increased average C/P composition of exported organic material compared to $Ctrl$. In $Acomb$, where the perturbation in wind stress is omitted, drawdown of CO_2

20   is smaller than in $GLcomb$, but still 14 % larger in $Acomb_{GAM}$ than in $Acomb_{RED}$ (56 and 63 ppm, respectively, see Fig. 6). Here, 12 out of the 14 % difference in pCO_2^{atm} can be attributed to a change in average C/P, thus almost the full extent of the change. As shown above, for the individual perturbation simulations, as well as for $GLcomb$, only half of the change in pCO_2^{atm} is due to changed average C/P. Thus, the effects of the perturbations do not add linearly.

4   Discussion

25   ### 4.1   Accounting for variable C/P in ocean carbon cycle models

The representation of ocean biology in GCMs tends to be over–simplified (Le Quéré et al., 2005a) and the development of the models is often held back by constraints imposed by maintaining the computational efficiency of the model. The Galbraith and Martiny (2015) model is simple and based on nutrient variables that are already present in biogeochemical models (nitrate and phosphate). By implementing the GAM parametrisation, or possibly a power law as that described by (Tanioka and

30   Matsumoto, 2017), an additional facet of the complexity of ocean biology can be implicitly accounted for at a relatively small computational cost. The approach taken by both Galbraith and Martiny (2015) and Tanioka and Matsumoto (2017) is to adapt

a function to all the available species–independent observations. This means that they account for the adaptation of plankton to the surrounding conditions, both in terms of species composition and individuals being more frugal in low nutrient conditions. This is one of the main advantages of such an approach, as it can be applied in a model without different plankton functional types, which is what we use here. Ganopolski and Brovkin (2017) appear to succeed with full glacial–interglacial CO_2 cycles

5 in CLIMBER-2, which does not have flexible stoichiometry for primary producers, but which has e.g. a temperature limitation on growth and explicit phyto- and zooplankton with different C uptake rates. This combination may perhaps achieve a similar response in carbon export in their simulations, when moving into a colder climate, as the flexible stoichiometry does in our simulations. The next step to approach a more realistic modelling of the biological pump would be to include a representation of preferential remineralisation of nutrients (e.g., Kolowith et al., 2001; Letscher and Moore, 2015), but this goes beyond the

10 scope of the present study.

One drawback of the Galbraith and Martiny (2015) approach is that it assumes that the C/P ratio continues to increase continuously with increasing $[PO_4]$. Thus, GAM does not account for the effects on C/P of temperature and light and the associated non–linear effects that could be of importance in e.g. the Southern Ocean (e.g., Yvon-Durocher et al., 2015; Tanioka and Matsumoto, 2017; Moreno et al., 2018), where $[PO_4]$ is very high. Up to $[PO_4] = 1.7\mu M$, the GAM parametrisation fits

15 the binned observational data well (see Fig. 1 and S2 Galbraith and Martiny, 2015). To account for the lack of observational data at higher $[PO_4]$, we have tested the effect of saturation of the C/P ratio at higher $[PO_4]$ in $Ctrl$ and $GLcomb$ simulations where we kept C/P = 55/1 at $[PO_4] > 1.7\mu M$. The increase in ocean carbon storage and decrease in pCO_2^{atm} between the $Ctrl$ and $GLcomb$ are nearly identical with GAM, thus saturation of the C/P ratio at very high $[PO_4]$ causes no noticable impact on our results.

20 **4.2 Implications of changed average C/P**

Part of the observed difference in pCO_2^{atm} between $GLcomb_{RED}$ and $GLcomb_{GAM}$ results from a difference in global average C/P in the control states ($Ctrl_{RED}$ and $Ctrl_{GAM}$). In $Ctrl_{GAM}$, the average C/P in the export production is close to 121/1, instead of 106/1 as in $Ctrl_{RED}$. We illustrate the consequences of this difference by running parallell simulations with fixed C/P of 121/1 (model version 121). Depending on the change in forcing, the simulations with 121 indicate that between

25 1/3 and 2/3 of the difference in drawdown between RED and GAM is due to a change in the average C/P (Fig. 6). This could have implications for model intercomparison projects, if they compare results from models that use different versions of fixed stoichiometry - e.g. models that apply Anderson and Sarmiento (1994) or Takahashi et al. (1985) stoichiometries, compared to those that use Redfield (1963). The problem with different stoichiometry assumptions in models is extensively discussed by Paulmier et al. (2009). Our study shows a direct consequence of such differences, with different model response

30 to the same perturbation. Note that $Ctrl_{GAM}$ has a larger inventory of DIC as well as C_{soft} compared to $Ctrl_{RED}$. Yet, the effect of applying the same perturbation results in a larger drawdown of CO_2 in GAM than in RED. This is opposite of the conclusions of Ödalen et al. (2018). The reason is that the flexible stoichiometry in effect increases the drawdown potential, which more than compensates for the increased carbon inventory in the control state. In $GLcomb_{GAM}$, the C/P in global

average export production increases from 121/1 to 134/1, which reflects the increased storage of organic carbon allowed by the flexible stoichiometry.

4.3 De–coupling of biologically sourced carbon and nutrient utilisation efficiency

Many studies have suggested increased ocean storage of organic carbon as a potentially important contributor to the low
5 glacial pCO_2^{atm} (e.g., Sarmiento and Toggweiler, 1984; Martin, 1990; Archer et al., 2000; Sigman and Boyle, 2000). However, biological production depends on water temperature (Eppley, 1972) and decreases in cold conditions. This temperature effect is parametrised in cGENIE as a local temperature–dependent uptake rate modifier proportional to $e^{(T/15.9°C)}$, and we see overall reduced productivity in our cold climate simulations (see e.g. LGM_{phy}, Table S.1.). As the climate cools, the temperature effect leads to a decrease in biological productivity and a subsequent decrease in $\overline{P^*}$ (see LGM_{phy} in Fig. 9). If productivity
10 decreases, other mechanisms are needed to offset this decrease, if the total ocean storage of organic carbon is to increase. Mechanisms that can contribute to increased deep ocean carbon retention are for example reduced SO overturning circulation (increased residence time of the AABW) and deeper remineralisation, which we apply through our perturbations in winds (Section 3.2.2) and RLS (Section 3.2.3). From our results, it is evident that variable stoichiometry can be another contributing factor. In our simulations, global average export production decreases, both in terms of POP (particulate organic phosporus)
15 and POC (particulate organic carbon), by 15 % between $Ctrl_{RED}$ and $GLcomb_{RED}$ because of the colder climate. However, the variable stoichiometry in GAM partly offsets this decrease in biological carbon capture - while the export production in terms of POP decreases by 17 %, the corresponding decrease in POC is only 10 %. Thus, in $GLcomb_{GAM}$ we achieve an increase in ocean inventory of remineralised carbon, which exceeds the one of $GLcomb_{RED}$ (Fig. 9).

Due to the competing effects between decreased export production and increased retention, the overall change in $\overline{P^*}$ is very
20 small when moving from the control state ($Ctrl$) to a glacial–like state ($GLcomb$) (Fig. 9). In the fixed stoichiometry case (RED), there is a small net increase in $\overline{P^*}$ of 0.020 in $GLcomb$ compared to $Ctrl$, which is linearly related to a small increase in storage of AC_{rem} in the ocean. In the case with variable stoichiometry (GAM), there is instead a very small decrease in $\overline{P^*}$ of 0003. With a linear response, we would thus expect a decrease in storage of AC_{rem} as well. Instead, we see a reasonably large increase in global average AC_{rem}.

25 This can be explained by the non–linearity introduced by the local variability in C/P. The reduced pCO_2^{atm} in $GLcomb$, compared to the control state 278 ppm, is partly due to the biological pump being more efficient in some key (HNLC) regions. In these regions, there is a reduction of the surface nutrient concentration in $GLcomb$ compared to $Ctrl$. When C/P increases with decreased surface layer P concentration, as it does in GAM, this further strengthens the biological pump in these key regions, resulting in a non–linear relationship between storage of remineralised phosphate and biologically sourced carbon
30 (Fig. 9). From this, we conclude that, in a system where stoichiometry is variable on a local scale, ocean storage of biologically sourced CO_2 can change while the amount of remineralised nutrients remains constant.

4.4 Implications of flexible C/P for deep ocean oxygen

As shown by e.g. Bradtmiller et al. (2010); Jaccard and Galbraith (2012); Galbraith and Jaccard (2015), deep ocean O_2 concentrations were lower during the LGM than in the Holocene. In our glacial–like states, we see a significant reduction of O_2 in both RED and GAM (Fig. 4 d and e), which is expected when we apply increased dust deposition and deeper remineralisation

5   (Galbraith and Jaccard, 2015). The reduction is stronger in GAM, due to the larger storage of respired carbon in this model version.

As illustrated by simulations in Galbraith and de Lavergne (2018), variable stoichiometry in itself is not always sufficient to achieve widespread deep ocean de–oxygenation in a model under glacial–like climate change. De–oxygenation is also dependent on e.g. deep water formation characteristics of the model (Galbraith and de Lavergne, 2018). It should be noted

10   that $Ctrl_{GAM}$ (Fig. 4 c) displays deeper oxygen minima in the oxygen minimum zones of both the Atlantic equatorial region and the North Pacific compared to what is seen in $Ctrl_{RED}$ (Fig. 4 b). In $Ctrl_{GAM}$, a large part of the interior North Pacific is anoxic (Fig. 4 c), while observations (Fig. 4 a) indicate very low oxygen levels, but not anoxia. If this parametrisation of variable stoichiometry is to be used in cGENIE in future studies, we suggest some re-tuning (e.g. by reducing the global average concentration of nutrients) to improve the representation of observed ocean oxygen concentrations in the modern control state.

15   ### 4.5 What can we learn from the model–data comparison of $\delta^{13}C$?

The model-data comparison in $\delta^{13}C$ (Section 3.1.4) suggests that the $Ctrl$ simulations are overall well correlated with Holocene benthic $\delta^{13}C$ data (HOL in Table S.3.). For the Atlantic, the correlation of the $Ctrl$ simulations is higher with the LGM benthic $\delta^{13}C$ (LGM in Table S.3.) than with HOL. However, the standard deviations (STDs) suggest that the Atlantic North–South gradient is not as strong as in an LGM ocean state and thus more similar to the modern ocean. When we apply

20   our combined forcings in the $GLcomb$ simulations, we achieve a stronger $\delta^{13}C$ gradient in the Atlantic, allowing for a closer match with LGM data in terms of STDs. A stronger gradient in $\delta^{13}C$ and more depleted suggest weaker ventilation of the deep ocean. The poor correlation in the Indo-Pacific, which we assume to be partly due to sparse mid-ocean observations for almost 70% of the ocean volume, makes the global statistics for LGM observations difficult to interpret.

Each of the two observational datasets (HOL and LGM) display similar correlations across the two model simulations. This

25   implies that our changes in forcings do not achieve any obvious changes in water mass distribution. The applied changes affect the chemical and biological conditions for ocean carbon storage, such as temperature and nutrient availability, more than the physical conditions, such as water mass volume and turnover time. To achieve a full glacial state with cGENIE, with a more glacial–like water mass distribution, additional physical forcings (freshwater, mixing etc.) are likely to be required. The very small differences between RED and GAM suggests that using variable stoichiometry does not impact our ability to achieve

30   the $\delta^{13}C$ patterns seen in observational data. However, we note that some retuning of the modern control state is recommended before cGENIE with variable stoichiometry is used in other studies.

5 Conclusions

In this paper, we examine the potential role of variable stoichiometry in biological production for glacial ocean CO_2 storage. We show that flexible C/P composition of organic matter allows a stronger response of pCO_2^{atm} to glacial–like changes in climate, remineralisation length scale and aeolian dust flux. We conclude that variable stoichiometry may be important for glacial

5 ocean CO_2 storage and for achieving the full extent of drawdown of atmospheric CO_2 in model simulations. In the experiment $GLcomb_{RED}$, with glacial–like climate and Redfield stoichiometry (Redfield, 1963), ocean carbon storage increases by 139 PgC and atmospheric CO_2 decreases by 64 ppm. In $GLcomb_{GAM}$, with glacial–like climate changes and variable stoichiometry, the corresponding numbers are 173 PgC and 80 ppm. Hence, the drawdown of atmospheric CO_2 increases by 25 % when C/P is variable.

10 About half of the increased drawdown of CO_2 results from different global average C/P in the export production. In addition, flexible stoichiometry allows increased carbon capture through the biological pump, while maintaining or even decreasing the fraction of remineralised to total nutrients in the deep ocean. With fixed stoichiometry, an increase in remineralised carbon is inevitably tied to a corresponding increase in remineralised nutrients.

We apply variable C/P parametrised as a simple function of the surface water concentration of PO_4, as suggested by Gal-

15 braith and Martiny (2015). Tanioka and Matsumoto (2017) suggest that it is unrealistic for C/P to continue to increase indefinitely with increased $[PO_4]$, and therefore suggest a more complex power law function, which takes into account saturation of the C/P ratio at high concentrations of PO_4. However, we found that saturation of the C/P ratio at concentrations higher than the observational upper bound of 1.7 μM causes no noticable impact on our results.

The representation of flexible stoichiometry used in this study (Galbraith and Martiny, 2015) can be used without large

20 increases in computational cost. It makes it possible to take into account, to first approximation, the complex biological changes that occur in the ocean during long–timescale climate change scenarios (see e.g. McInerney and Wing, 2011). We show here that, for glacial–interglacial cycles, this complexity contributes to changes in atmospheric CO_2 through flexible C/P ratios.

Biogeosciences
Discussions

Open Access

EGU

Appendix A: Regenerated acidic carbon

Carbon enters the ocean mainly in the form of CO_2 and dissolved carbonate. Despite this, the major fraction of carbon in the ocean resides as bicarbonate ions. The source related state variables acidic and basic carbon (AC and BC, respectively) allow

5 us to separate the ocean DIC inventory into the sources of CO_2 (AC) and dissolved carbonate (BC). The concept of the sourced related state variables was first described by Walin et al. (2014).

AC and BC are defined from DIC and alkalinity (ALK) as

$$AC = DIC - \frac{1}{2}ALK \tag{A1}$$
$$BC = \frac{1}{2}ALK \tag{A2}$$

10 Total AC and BC include all ocean sources of carbon, including e.g. river runoff, air–sea gas exchange, the biological pump etc.

To isolate the CO_2 that was supplied to the ocean via biological soft tissue, we make use of the separation of DIC and ALK into their preformed and remineralised fractions (see Section 2.5). Thus, we then compute the remineralised acidic carbon (AC_{rem}) as

15 $$AC_{rem} = DIC_{rem} - \frac{1}{2}ALK_{rem} \tag{A3}$$

Author contributions. M. Ödalen, J. Nycander, K. I. C. Oliver and A. Ridgwell designed the model experiments. A. Ridgwell developed the original cGENIE model code. M. Ödalen and K. I. C. Oliver adapted the model code and forcings for the experimental design. M. Ödalen performed the model simulations and produced the tables and figures. C. D. Peterson provided expertise on ocean $\delta^{13}C$ analysis. M. Ödalen prepared the manuscript with contributions from all co–authors.

20 *Competing interests.* No competing interests are present.

Biogeosciences
Discussions

References

Anderson, L. A. and Sarmiento, J. L.: Redfield ratios of remineralization determined by nutrient data analysis, Global biogeochemical cycles, 8, 65–80, 1994.

Archer, D., Winguth, A., Lea, D., and Mahowald, N.: What caused the glacial/interglacial atmospheric pCO_2 cycles?, Reviews of Geophysics, 38, 159–189, 2000.

5 Boyle, E. A. and Keigwin, L.: North Atlantic thermohaline circulation during the past 20,000 years linked to high-latitude surface temperature, Nature, 330, 35, 1987.

Bradtmiller, L., Anderson, R., Sachs, J., and Fleisher, M.: A deeper respired carbon pool in the glacial equatorial Pacific Ocean, Earth and Planetary Science Letters, 299, 417–425, 2010.

Broecker, W. S.: Glacial to interglacial changes in ocean chemistry, Progress in Oceanography, 11, 151–197,
10 https://doi.org/http://dx.doi.org/10.1016/0079-6611(82)90007-6, http://www.sciencedirect.com/science/article/pii/0079661182900076, 1982a.

Broecker, W. S.: Ocean chemistry during glacial time, Geochimica et Cosmochimica Acta, 46, 1689–1705, 1982b.

Brovkin, V., Ganopolski, A., Archer, D., and Rahmstorf, S.: Lowering of glacial atmospheric CO_2 in response to changes in oceanic circulation and marine biogeochemistry, Paleoceanography, 22, PA4202, 2007.

15 cGENIE GitHub repository: https://github.com/derpycode, 2019.

cGENIE release 1.9.1b: https://doi.org/10.5281/zenodo.1407658, https://github.com/derpycode/muffindoc/releases/tag/1.9.1b, 2018.

cGENIE release v0.9.5: https://doi.org/10.5281/zenodo.3235761, https://github.com/derpycode/cgenie.muffin/releases/tag/v0.9.5, 2019.

Chikamoto, M., Abe-Ouchi, A., Oka, A., and Smith, S. L.: Temperature-induced marine export production during glacial period, Geophysical Research Letters, 39, 2012.

20 Ciais, P., Sabine, C., Bala, G., Bopp, L., Brovkin, V., Canadell, J., Chhabra, A., DeFries, R., Galloway, J., Heimann, M., Jones, C .and Le Quéré, C., Myeni, R. B., Piao, S., and Thornton, P.: Carbon and other biogeochemical cycles, in: Climate Change 2013: The Physical Science Basis. Contribution of Working Group I to the Fifth Assessment Report of the Intergovernmental Panel on Climate Change, edited by Stocker, T. F., Qin, D., Plattner, G. K., Tignor, M., Allen, S. K., Boschung, J., Nauels, A., Xia, Y., Bex, V., and Midgley, P. M., chap. 6, pp. 465–570, Cambridge University Press, Cambridge, United Kingdom and New York, NY, USA, 2013.

25 Curry, W. B. and Oppo, D. W.: Glacial water mass geometry and the distribution of δ13C of ΣCO2 in the western Atlantic Ocean, Paleoceanography, 20, 2005.

Curry, W. B., Duplessy, J.-C., Labeyrie, L., and Shackleton, N. J.: Changes in the distribution of δ13C of deep water ΣCO2 between the last glaciation and the Holocene, Paleoceanography and Paleoclimatology, 3, 317–341, 1988.

Davies-Barnard, T., Ridgwell, A., Singarayer, J., and Valdes, P.: Quantifying the influence of the terrestrial biosphere on glacial–interglacial
30 climate dynamics, Climate of the Past, 13, 1381–1401, https://doi.org/10.5194/cp-13-1381-2017, https://www.clim-past.net/13/1381/2017/, 2017.

Duplessy, J., Shackleton, N., Fairbanks, R., Labeyrie, L., Oppo, D., and Kallel, N.: Deepwater source variations during the last climatic cycle and their impact on the global deepwater circulation, Paleoceanography, 3, 343–360, 1988.

Eggleston, S. and Galbraith, E. D.: The devil's in the disequilibrium: sensitivity of ocean carbon storage to climate state and iron fertilization
35 in a general circulation model, Biogeosciences, 2018.

Eppley, R. W.: Temperature and phytoplankton growth in the sea, Fish. bull, 70, 1063–1085, 1972.

Galbraith, E. and de Lavergne, C.: Response of a comprehensive climate model to a broad range of external forcings: relevance for deep ocean ventilation and the development of late Cenozoic ice ages, Climate Dynamics, pp. 1–27, 2018.

Galbraith, E. D. and Jaccard, S. L.: Deglacial weakening of the oceanic soft tissue pump: global constraints from sedimentary nitrogen isotopes and oxygenation proxies, Quaternary Science Reviews, 109, 38–48, 2015.

Galbraith, E. D. and Martiny, A. C.: A simple nutrient-dependence mechanism for predicting the stoichiometry of marine ecosystems, Proceedings of the National Academy of Sciences, 112, 8199–8204, 2015.

Ganopolski, A. and Brovkin, V.: Simulation of climate, ice sheets and CO2 evolution during the last four glacial cycles with an Earth system model of intermediate complexity, Climate of the Past, 13, 1695–1716, 2017.

Garcia, H. E., Locarnini, R. A., Boyer, T. P., Antonov, J. I., Baranova, O., Zweng, M. M., Reagan, J. R., and D.R., J.: World Ocean Atlas 2013, Volume 4: Dissolved Inorganic Nutrients (phosphate, nitrate, silicate), Tech. Rep. 76, NOAA Atlas NESDIS, 25 pp., 2014a.

Garcia, H. E., Locarnini, R. A., Boyer, T. P., Antonov, J. I., Baranova, O., Zweng, M. M., Reagan, J. R., and R., J. D.: World Ocean Atlas 2013, Volume 3: Dissolved Oxygen, Apparent Oxygen Utilization, and Oxygen Saturation), Tech. Rep. 75, NOAA Atlas NESDIS, 27 pp., 2014b.

Gebbie, G., Peterson, C. D., Lisiecki, L. E., and Spero, H. J.: Global-mean marine δ13C and its uncertainty in a glacial state estimate, Quaternary Science Reviews, 125, 144–159, 2015.

Griffies, S. M.: The Gent–McWilliams skew flux, Journal of Physical Oceanography, 28, 831–841, 1998.

Hain, M. P., Sigman, D. M., and Haug, G. H.: Carbon dioxide effects of Antarctic stratification, North Atlantic Intermediate Water formation, and subantarctic nutrient drawdown during the last ice age: Diagnosis and synthesis in a geochemical box model, Global Biogeochemical Cycles, 24, 2010.

Headly, M. A. and Severinghaus, J. P.: A method to measure Kr/N2 ratios in air bubbles trapped in ice cores and its application in reconstructing past mean ocean temperature, Journal of Geophysical Research: Atmospheres, 112, D19 105, https://doi.org/10.1029/2006JD008317, http://dx.doi.org/10.1029/2006JD008317, d19105, 2007.

Ito, T. and Follows, M. J.: Preformed phosphate, soft tissue pump and atmospheric CO_2, Journal of Marine Research, 63, 813–839, 2005.

Jaccard, S. L. and Galbraith, E. D.: Large climate-driven changes of oceanic oxygen concentrations during the last deglaciation, Nature Geoscience, 5, 151, 2012.

Kohfeld, K., Graham, R., De Boer, A., Sime, L., Wolff, E., Le Quéré, C., and Bopp, L.: Southern Hemisphere westerly wind changes during the Last Glacial Maximum: paleo-data synthesis, Quaternary Science Reviews, 68, 76–95, 2013.

Kohfeld, K. E. and Ridgwell, A.: Glacial-Interglacial Variability in Atmospheric CO_2, in: Surface Ocean-Lower Atmosphere Processes, edited by Le Quéré, C. and S., S. E., pp. 251–286, American Geophysical Union, Washington D.C., 2009.

Kohfeld, K. E., Le Quéré, C., Harrison, S. P., and Anderson, R. F.: Role of marine biology in glacial-interglacial CO2 cycles, Science, 308, 74–78, 2005.

Kolowith, L. C., Ingall, E. D., and Benner, R.: Composition and cycling of marine organic phosphorus, Limnology and Oceanography, 46, 309–320, 2001.

Kumar, N., Anderson, R., Mortlock, R., Froelich, P., Kubik, P., Dittrich-Hannen, B., and Suter, M.: Increased biological productivity and export production in the glacial Southern Ocean, Nature, 378, 675, 1995.

Kwon, E. Y., Primeau, F., and Sarmiento, J. L.: The impact of remineralization depth on the air–sea carbon balance, Nature Geoscience, 2, 630–635, 2009.

Lauderdale, J. M., Garabato, A. C. N., Oliver, K. I. C., Follows, M. J., and Williams, R. G.: Wind-driven changes in Southern Ocean residual circulation, ocean carbon reservoirs and atmospheric CO_2, Climate dynamics, 41, 2145–2164, 2013.

Le Quéré, C., Harrison, S. P., Colin Prentice, I., Buitenhuis, E. T., Aumont, O., Bopp, L., Claustre, H., Cotrim Da Cunha, L., Geider, R., Giraud, X., et al.: Ecosystem dynamics based on plankton functional types for global ocean biogeochemistry models, Global Change Biology, 11, 2016–2040, 2005a.

5 Le Quéré, C., Harrison, S. P., Colin Prentice, I., Buitenhuis, E. T., Aumont, O., Bopp, L., Claustre, H., Cotrim Da Cunha, L., Geider, R., Giraud, X., et al.: Ecosystem dynamics based on plankton functional types for global ocean biogeochemistry models, Global Change Biology, 11, 2016–2040, 2005b.

Letscher, R. T. and Moore, J. K.: Preferential remineralization of dissolved organic phosphorus and non-Redfield DOM dynamics in the global ocean: Impacts on marine productivity, nitrogen fixation, and carbon export, Global Biogeochemical Cycles, 29, 325–340, 2015.

10 Locarnini, R. A., Mishonov, A. V., Antonov, J. I., Boyer, T. P., Garcia, H. E., Baranova, O. K., Zweng, M. M., Paver, C. R., Reagan, J. R., Johnson, D. R., Hamilton, M., and Seidov, D.: World Ocean Atlas 2013, Volume 1: Temperature, Tech. Rep. 73, NOAA Atlas NESDIS, 40 pp., 2013.

Mahowald, N. M., Muhs, D. R., Levis, S., Rasch, P. J., Yoshioka, M., Zender, C. S., and Luo, C.: Change in atmospheric mineral aerosols in response to climate: Last glacial period, preindustrial, modern, and doubled carbon dioxide climates, Journal of Geophysical Research:

15 Atmospheres, 111, D10 202, https://doi.org/10.1029/2005JD006653, http://dx.doi.org/10.1029/2005JD006653, 2006.

Marinov, I., Gnanadesikan, A., Toggweiler, J., and Sarmiento, J.: The southern ocean biogeochemical divide, Nature, 441, 964, 2006.

Marinov, I., Gnanadesikan, A., Sarmiento, J. L., Toggweiler, J. R., Follows, M., and Mignone, B. K.: Impact of oceanic circulation on biological carbon storage in the ocean and atmospheric pCO_2, Global Biogeochemical Cycles, 22, 2008.

Marsh, R., Müller, S., Yool, A., and Edwards, N.: Incorporation of the C-GOLDSTEIN efficient climate model into the GENIE frame-

20 work:"eb_go_gs" configurations of GENIE, Geoscientific Model Development, 4, 957–992, 2011.

Martin, J. H.: Glacial-interglacial CO2 change: The iron hypothesis, Paleoceanography, 5, 1–13, 1990.

Matsumoto, K.: Biology-mediated temperature control on atmospheric pCO_2 and ocean biogeochemistry, Geophysical Research Letters, 34, 2007.

Matsumoto, K., Oba, T., Lynch-Stieglitz, J., and Yamamoto, H.: Interior hydrography and circulation of the glacial Pacific Ocean, Quaternary

25 Science Reviews, 21, 1693–1704, 2002.

McCarthy, G., Smeed, D., Johns, W. E., Frajka-Williams, E., Moat, B., Rayner, D., Baringer, M., Meinen, C., Collins, J., and Bryden, H.: Measuring the Atlantic meridional overturning circulation at 26 N, Progress in Oceanography, 130, 91–111, 2015.

McInerney, F. A. and Wing, S. L.: The Paleocene-Eocene Thermal Maximum: A perturbation of carbon cycle, climate, and biosphere with implications for the future, Annual Review of Earth and Planetary Sciences, 39, 489–516, 2011.

30 Menviel, L., Joos, F., and Ritz, S.: Simulating atmospheric CO_2, ^{13}C and the marine carbon cycle during the Last Glacial–Interglacial cycle: possible role for a deepening of the mean remineralization depth and an increase in the oceanic nutrient inventory, Quaternary Science Reviews, 56, 46–68, 2012.

Menviel, L., Yu, J., Joos, F., Mouchet, A., Meissner, K., and England, M.: Poorly ventilated deep ocean at the Last Glacial Maximum inferred from carbon isotopes: A data-model comparison study, Paleoceanography and Paleoclimatology, 32, 2–17, 2017.

35 Moreno, A. R., Hagstrom, G. I., Primeau, F. W., Levin, S. A., and Martiny, A. C.: Marine phytoplankton stoichiometry mediates nonlinear interactions between nutrient supply, temperature, and atmospheric CO_2, Biogeosciences, 15, 2761, 2018.

Muglia, J., Skinner, L. C., and Schmittner, A.: Weak overturning circulation and high Southern Ocean nutrient utilization maximized glacial ocean carbon, Earth and Planetary Science Letters, 496, 47–56, 2018.

Ödalen, M., Nycander, J., Oliver, K. I. C., Brodeau, L., and Ridgwell, A.: The influence of the ocean circulation state on ocean carbon storage and CO_2 drawdown potential in an Earth system model, Biogeosciences, 15, 1367–1393, https://doi.org/10.5194/bg-15-1367-2018, https://www.biogeosciences.net/15/1367/2018/, 2018.

5 Paulmier, A., Kriest, I., and Oschlies, A.: Stoichiometries of remineralisation and denitrification in global biogeochemical ocean models, Biogeosciences, 6, 923–935, 2009.

Peterson, C. D., Lisiecki, L. E., and Stern, J. V.: Deglacial whole-ocean $\delta 13C$ change estimated from 480 benthic foraminiferal records, Paleoceanography, 29, 549–563, 2014.

Petit, J.-R., Jouzel, J., Raynaud, D., Barkov, N. I., Barnola, J.-M., Basile, I., Bender, M., Chappellaz, J., Davis, M., Delaygue, G., et al.:
10 Climate and atmospheric history of the past 420,000 years from the Vostok ice core, Antarctica, Nature, 399, 429–436, 1999.

Redfield, A. C.: The influence of organisms on the composition of sea–water, The Sea, 2, 26–77, 1963.

Ridgwell, A., Hargreaves, J. C., Edwards, N. R., Annan, J. D., Lenton, T. M., Marsh, R., Yool, A., and Watson, A.: Marine geochemical data assimilation in an efficient Earth System Model of global biogeochemical cycling, Biogeosciences, 4, 87–104, 2007.

Sarmiento, J. and Toggweiler, J.: A new model for the role of the oceans in determining atmospheric pCO_2, Nature, 308, 621–624, 1984.

15 Shackleton, N.: Carbon-13 in Uvigerina: Tropical rain forest history and the equatorial Pacific carbonate dissolution cycle, The fate of fossil fuel CO_2 in the oceans, pp. 401–428, 1977.

Sigman, D. M. and Boyle, E. A.: Glacial/interglacial variations in atmospheric carbon dioxide, Nature, 407, 859–869, 2000.

Sigman, D. M., Hain, M. P., and Haug, G. H.: The polar ocean and glacial cycles in atmospheric CO_2 concentration, Nature, 466, 47–55, 2010.

20 Sime, L. C., Kohfeld, K. E., Le Quéré, C., Wolff, E. W., de Boer, A. M., Graham, R. M., and Bopp, L.: Southern Hemisphere westerly wind changes during the Last Glacial Maximum: model-data comparison, Quaternary Science Reviews, 64, 104–120, 2013.

Sime, L. C., Hodgson, D., Bracegirdle, T. J., Allen, C., Perren, B., Roberts, S., and de Boer, A. M.: Sea ice led to poleward-shifted winds at the Last Glacial Maximum: the influence of state dependency on CMIP5 and PMIP3 models, Climate of the Past, 12, 2241–2253, 2016.

Stephens, B. B. and Keeling, R. F.: The influence of Antarctic sea ice on glacial–interglacial CO 2 variations, Nature, 404, 171, 2000.

25 Tagliabue, A., Aumont, O., DeAth, R., Dunne, J. P., Dutkiewicz, S., Galbraith, E., Misumi, K., Moore, J. K., Ridgwell, A., Sherman, E., et al.: How well do global ocean biogeochemistry models simulate dissolved iron distributions?, Global Biogeochemical Cycles, 30, 149–174, 2016.

Takahashi, T., Broecker, W. S., and Langer, S.: Redfield ratio based on chemical data from isopycnal surfaces, Journal of Geophysical Research: Oceans, 90, 6907–6924, 1985.

30 Tanioka, T. and Matsumoto, K.: Buffering of ocean export production by flexible elemental stoichiometry of particulate organic matter, Global Biogeochemical Cycles, 31, 1528–1542, 2017.

Walin, G., Hieronymus, J., and Nycander, J.: Source-related variables for the description of the oceanic carbon system, Geochemistry, Geophysics, Geosystems, 15, 3675–3687, 2014.

Watson, A. J., Bakker, D., Ridgwell, A., Boyd, P., and Law, C.: Effect of iron supply on Southern Ocean CO 2 uptake and implications for
35 glacial atmospheric CO 2, Nature, 407, 730, 2000.

Yvon-Durocher, G., Dossena, M., Trimmer, M., Woodward, G., and Allen, A. P.: Temperature and the biogeography of algal stoichiometry, Global Ecology and Biogeography, 24, 562–570, 2015.
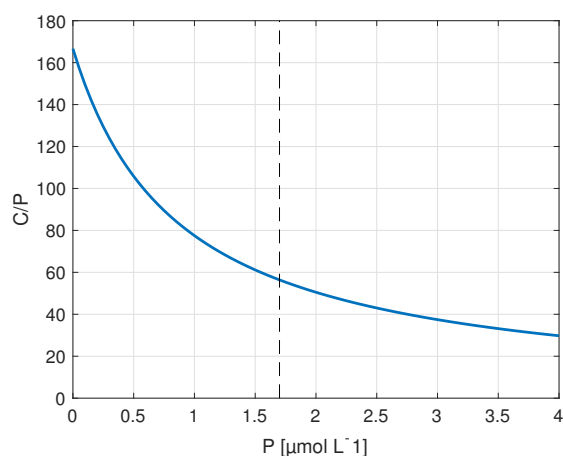
Figure 1. Flexible stoichiometry C/P (y-axis) dependent on the P-concentration [$\mu mol L^{-1}$] (x-axis), as described by Eq. 1. Here, we extend the relationship beyond the observational interval 0–1.7 $\mu mol L^{-1}$ (bounded by dashed line) which form the basis of the relation derived by Galbraith and Martiny (2015).
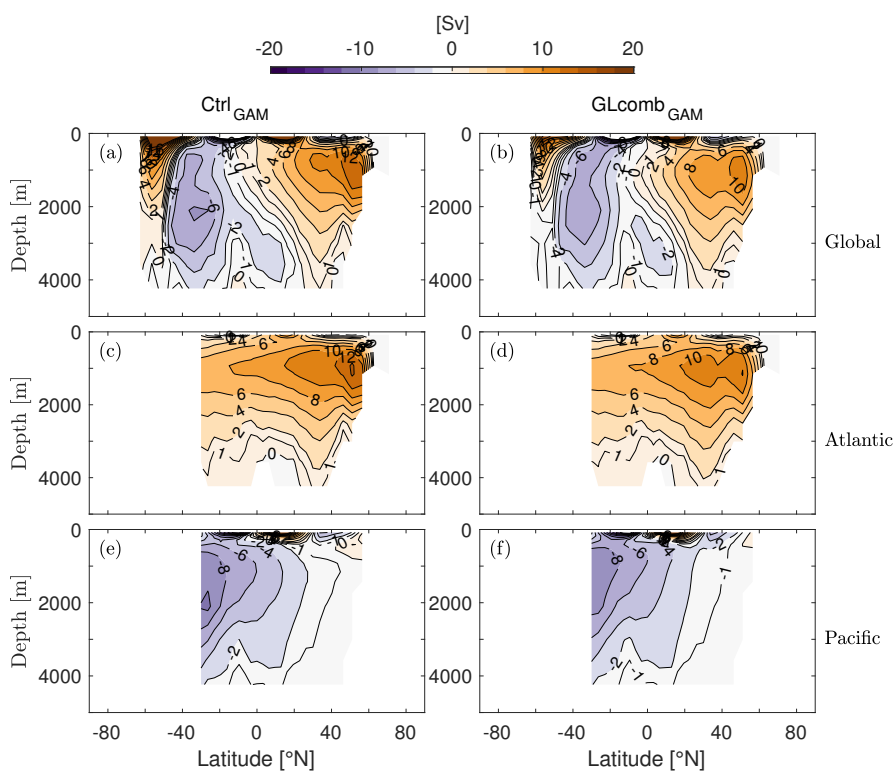
Figure 2. The eulerian component of the Global (panels a, b), Atlantic (panels c, d) , and Pacific (panels e, f) ocean meridional overturning streamfunction (1 Sv = $10^6 m^3 s^{-1}$) of $Ctrl_{GAM}$ (panels a, c, e) and $GLcomb_{GAM}$ (panels b, d, f). Note that the eddy–induced transport of tracers is taken into account through a skew–diffusive flux (Griffies, 1998) that is present in the velocity fields used to compute the eulerian stream function.
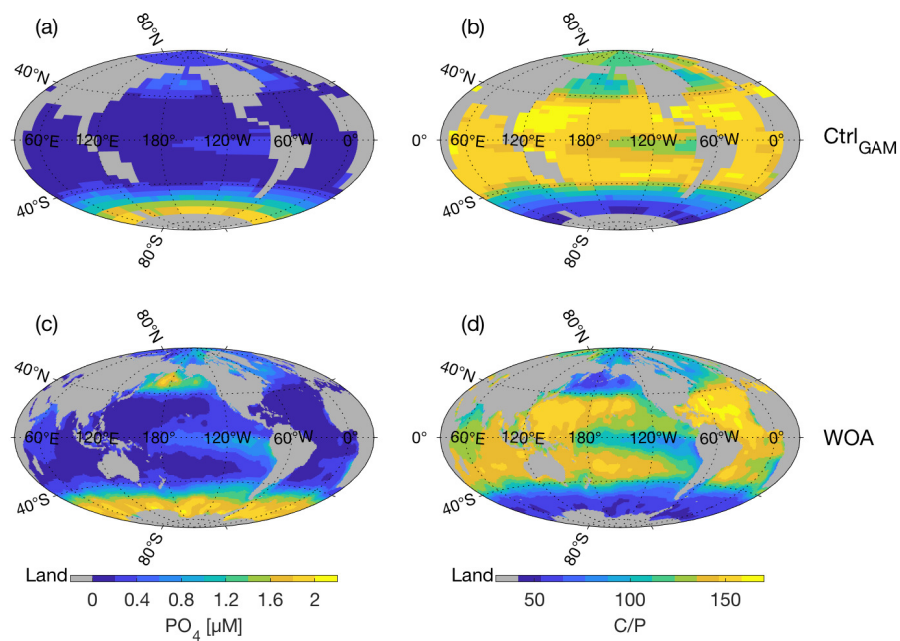
Figure 3. Surface PO_4 concentration (μM) (left hand column) and corresponding C/P as calculated using parametrisation of Galbraith and Martiny (2015) (right column). Panels show in $Ctrl_{GAM}$ (a, b) and observations (World Ocean Atlas 2013, Garcia et al., 2014a) (c, d).
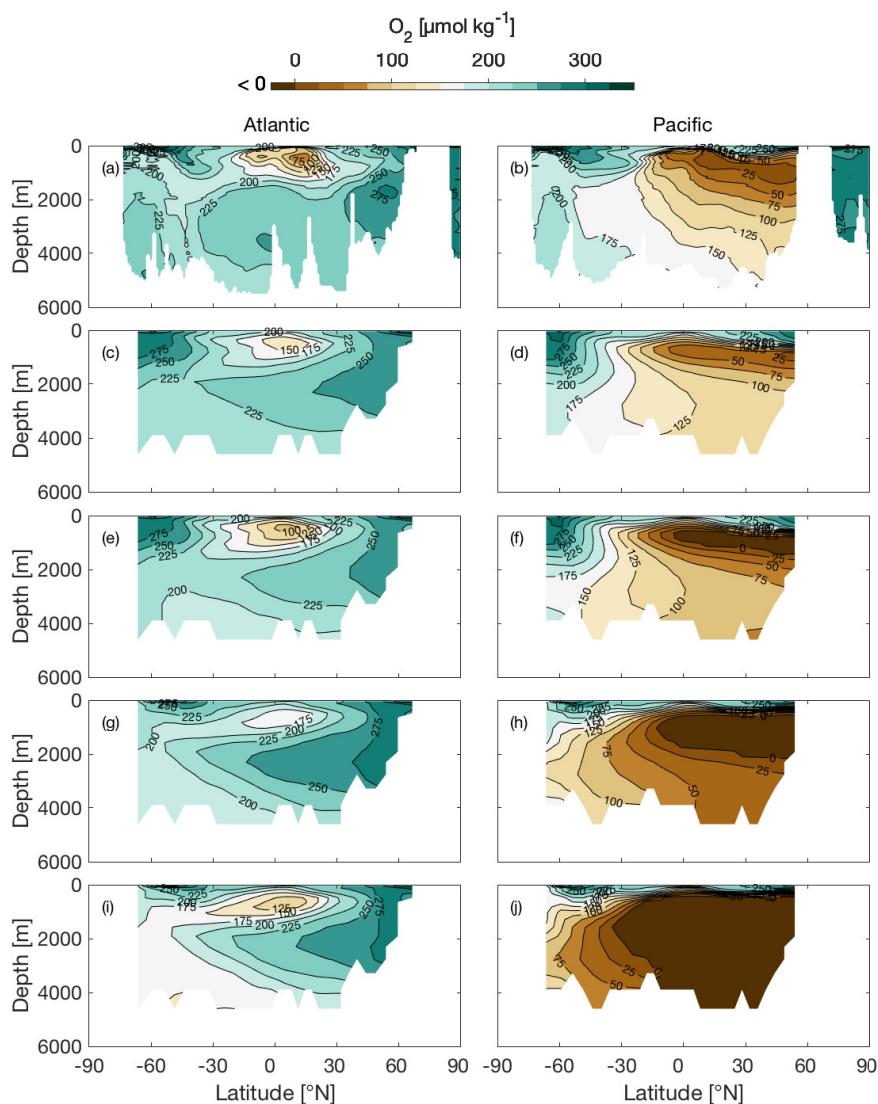
Figure 4. Sections of O_2 concentration ($\mu mol\,kg^{-1}$) along 25 °W in the Atlantic basin (left hand column) and along 135 °W in the Pacific basin (right hand column). Panels show observations (World Ocean Atlas 2013, Garcia et al., 2014b) (a, b), and model states $Ctrl_{RED}$ (c, d), $Ctrl_{GAM}$ (e, f), $GLcomb_{RED}$ (g, h) and $GLcomb_{GAM}$ (i, j).
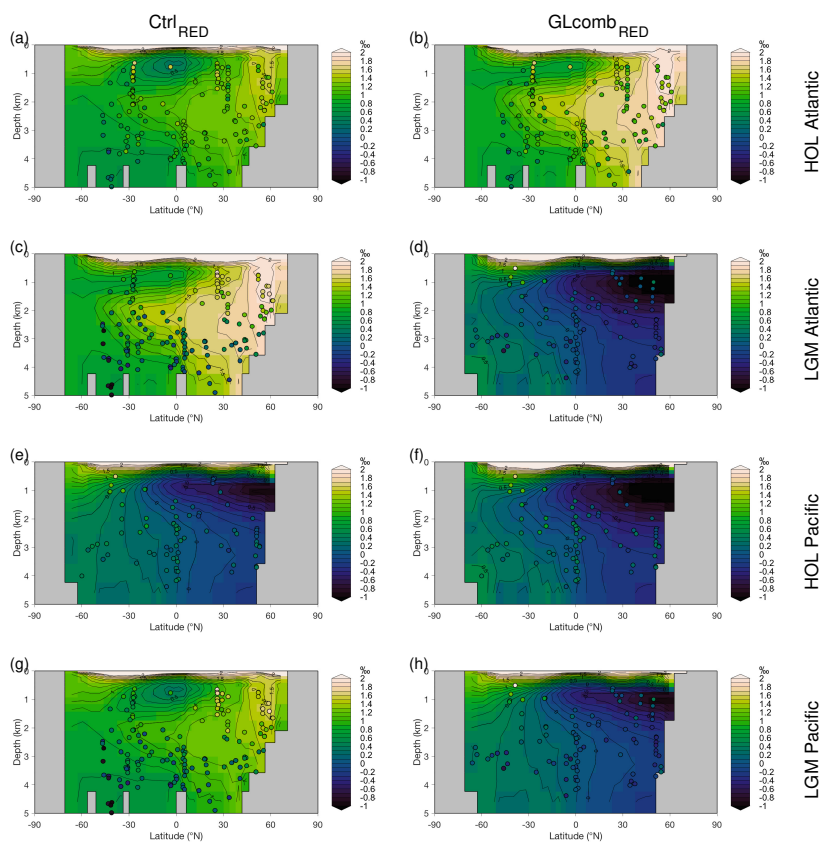
Figure 5. Model ocean $\delta^{13}C$ (contours) compared to the two time slices (HOL and LGM) of observed benthic $\delta^{13}C$ (circles) of Peterson et al. (2014). Left hand column shows $Ctrl_{RED}$ (panels a, c, e, g) and right hand column shows $GLcomb_{RED}$ (panels b, d, f, h). The rows show, from top to bottom, a-b) HOL Atlantic, c-d) LGM Atlantic, e-f) HOL Pacific, g-h) LGM Pacific. Note that, when we compare $GLcomb_{RED}$ to LGM observations (panels d and h), a constant of 0.32 ‰ is subtracted from $GLcomb_{RED}$ data, to account for terrestrial release of $\delta^{13}C$–depleted terrestrial carbon. The corresponding comparison for model version GAM is shown in Fig. S.3.
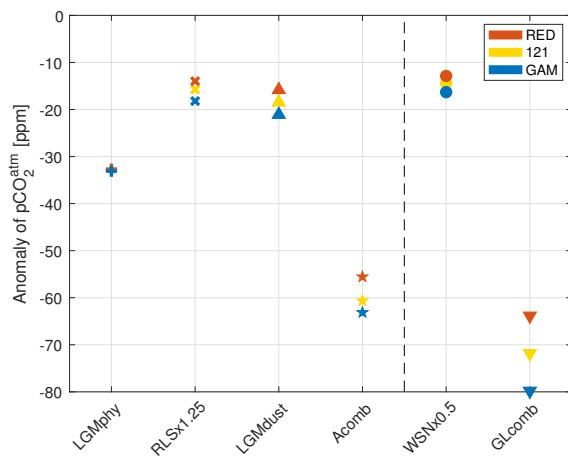
Figure 6. Resulting CO_2 anomaly, with respect to the control state 278 ppm, of the sensitivity experiments $LGMphy$ (plus–symbol), $RLS \times 1.25$ (×–symbol), $LGMdust$ (upward arrowheads), and $WSN \times 0.5$ (circles), and of the combined experiments $Acomb$ (stars) and $GLcomb$ (downward arrowheads). Results of the different model versions RED, 121 and GAM are shown in red, yellow and blue, respectively. The vertical dashed line separates simulations without (left) and with (right) wind perturbation.
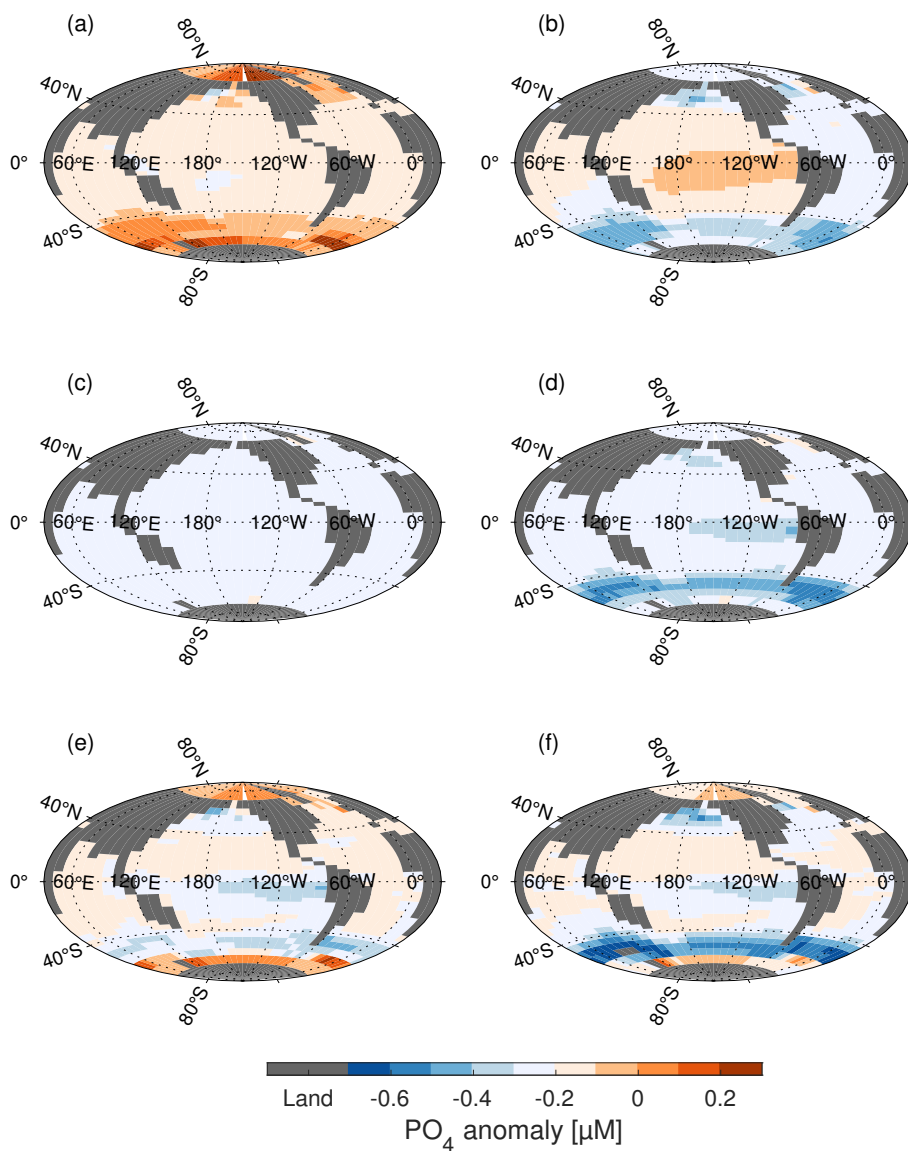
Figure 7. Surface PO_4 anomaly $[\mu M]$, with respect to surface concentration of PO_4 in $Ctrl_{GAM}$ (Fig. 3a), for a) $LGMphy_{GAM}$, b) $WSN \times 0.5_{GAM}$ c) $RLS \times 1.25_{GAM}$, d) $LGMdust_{GAM}$, e) $Acomb_{GAM}$, f) $GLcomb_{GAM}$. Changes in surface nutrient fields are similar for all three model versions (RED, GAM, 121), thus only GAM is shown.
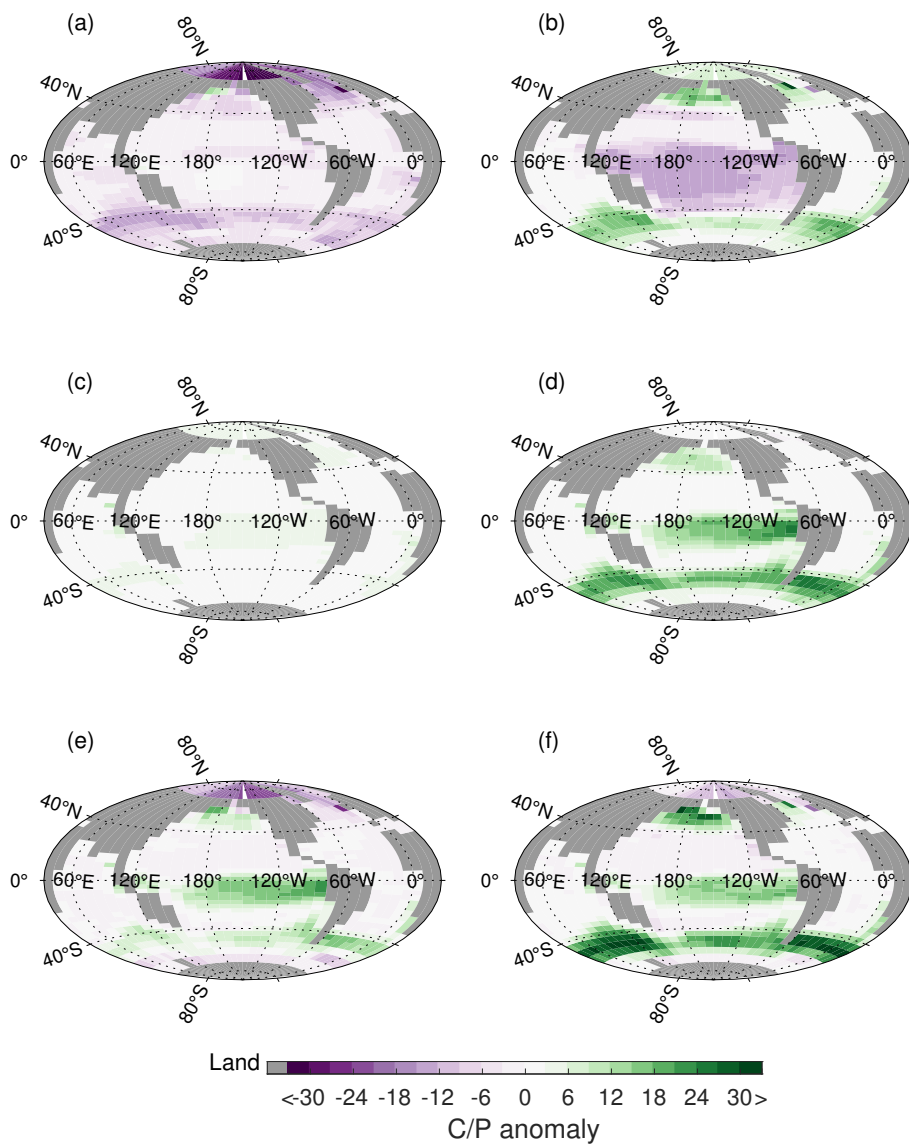
Figure 8. Surface C/P anomaly, with respect to C/P of $Ctrl_{GAM}$ (Fig. 3b), for a) $LGMphy_{GAM}$, b) $WSN \times 0.5_{GAM}$ c) $RLS \times 1.25_{GAM}$, d) $LGMdust_{GAM}$, e) $Acomb_{GAM}$, f) $GLcomb_{GAM}$.
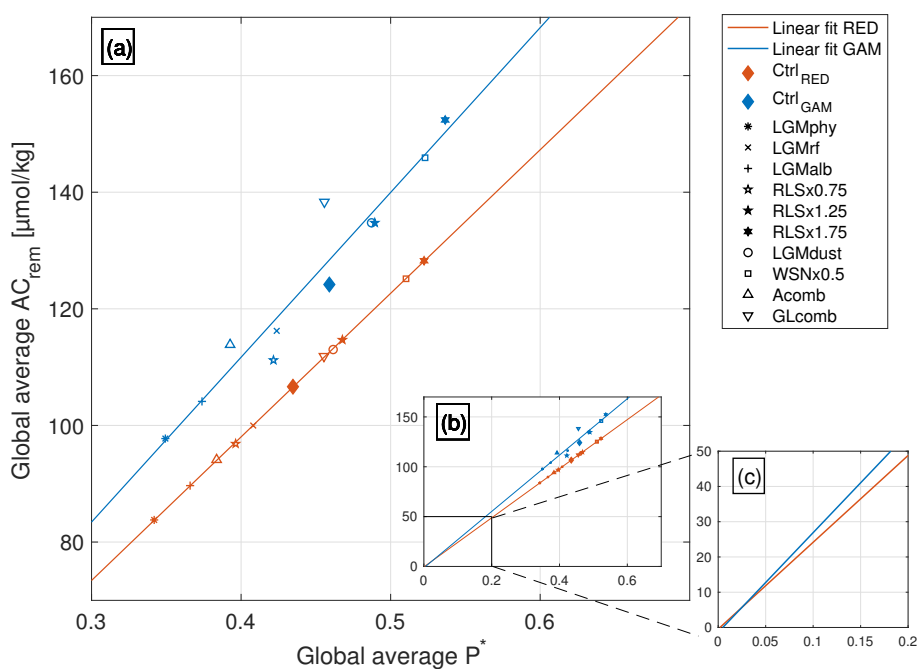
Figure 9. Remineralised acidic carbon ($AC_{rem} = DIC_{rem} - (1/2) * ALK_{rem}$, see Appendix A) as a function of $\overline{P^*}$. Simulations using model versions RED and GAM are shown in red and blue, respectively. Different symbols indicate the sensitivity experiments, listed in the panel on the right hand side. Red and blue lines show linear least–squares fits to the separate ensembles for RED and GAM. Panels illustrate a) the deviation from the least–squares fit of the GAM ensemble as opposed to the RED ensemble, b) the linear fits extrapolated to origo, and c) a zoom–in around the origin, where the RED (red) line goes through the origin, while the GAM (blue) does not.

Table 1. List of experiments. Ensemble member acronyms, short descriptions of what the simulation tests, and specifications of parameter settings for each ensemble member. The pCO_2^{atm} is either prescribed to pre-industrial (PI) = 278 ppm, or freely varying with changes in climate and ocean circulation. The radiative forcing is either coupled to the pCO_2^{atm} of the atmospheric chemistry module of the model, or fixed at a value corresponding $pCO_2^{atm} = 185$ ppm. The zonal albedo profile is either representative of modern/PI conditions or of the LGM. The wind stress is either modern/PI, or has an adjusted peak in wind stress at $\pm50°$ N. The modern/PI remineralisation length scale (RLS) is 590 m. If RLS is changed, it is multiplied by a factor fr. Dust forcing is either modern/PI or representative of LGM. Each experiment is conducted using model versions witg C/P fixed at 106/1 (Redfield, 1963, , denoted RED), C/P variable with surface ocean PO_4 concentration (Galbraith and Martiny, 2015, denoted $GM15$), and C/P fixed at 121/1 (denoted 121, see Section 2.3).

Ensemble member	Short description	pCO_2^{atm}	Radiative forcing	Zonal albedo	Wind stress[1] at $\pm50°$N	RLS[2] (m)	Dust forcing
Ctrl	Control	278 ppm (restored)	coupled to pCO_2^{atm}	modern/PI	modern/PI	590	modern/PI
LGMrf	LGM radiative forcing	variable	fixed at 185 ppm	modern/PI	modern/PI	590	modern/PI
LGMalb	LGM zonal albedo	variable	coupled to pCO_2^{atm}	LGM[3]	modern/PI	590	modern/PI
LGMphy	*LGMrf*+*LGMalb*	variable	fixed at 185 ppm	LGM	modern/PI	590	modern/PI
WNS×0.5	Wind stress at ±50°N reduced	variable	coupled to pCO_2^{atm}	modern/PI	PI ×0.5	590	modern/PI
RLS×fr[1]	RLS changed by factor *fr*	variable	coupled to pCO_2^{atm}	modern/PI	modern/PI	590 × *fr*	modern/PI
LGMdust	LGM dust flux	variable	coupled to pCO_2^{atm}	modern/PI	modern/PI	590	LGM[4]
GLcomb	"Glacial-like" (GL) (all forcings)	variable	fixed at 185 ppm	LGM	PI ×0.5	590 × 1.25	LGM
Acomb	"GL" with PI wind	variable	fixed at 185 ppm	LGM	modern/PI	590 × 1.25	LGM

1) See Lauderdale et al. (2013) for example of reduced wind profile for the Southern Hemisphere.

2) *fr* = multiplication factor for remineralisation length scale. We test multiplication factors between 0.75 and 1.75, corresponding to a change in RLS between -25 % to +75 %.

3) Calculated from HADCM3 LGM (21ka) simulation of Davies-Barnard et al. (2017)

4) Re-gridded LGM dust flux from Mahowald et al. (2006)

Table 2. Atmospheric CO_2 (pCO_2^{atm}, ppm), global ocean averages of temperature ($\overline{T_{oce}}$, °C), $\overline{P^*}$ and $\overline{O_2}$ ($\mu mol\ kg^{-1}$), and Atlantic overturning streamfunction (ψ, Sverdrups (SV)) maximum and minimum, for observations, and for selected ensemble members in each model version (RED/GAM). Observed modern day $\overline{T_{oce}}$ and $\overline{O_2}$ was computed using the World Ocean Atlas 2013 (Locarnini et al., 2013; Garcia et al., 2014b). $\overline{P^*}$ for the modern day ocean is estimated by Ito and Follows (2005). Average modern day AMOC strength is estimated by McCarthy et al. (2015) from the RAPID-MOCHA array at 26 °N (corresponding to Atlantic ψ_{max} in the model). Note that observed pCO_2^{atm} is given for pre-industrial (PI) climate, as we do not model anthropogenic release of CO_2.

Ensemble member	pCO_2^{atm} (ppm)	$\overline{T_{oce}}$ (°C)	$\overline{P^*}$	$\overline{O_2}$ ($\mu mol\ kg^{-1}$)	Atlantic ψ_{max} (Sv)	Atlantic ψ_{min} (SV)
Obs. modern	278 (PI)	3.49	0.36	169	17.2±0.9	-
Ensemble member	version RED / GAM					
Ctrl	278.0 / 278.0	3.56 / 3.56	0.43 / 0.46	166 / 144	14.2 / 14.3	-0.8 / -0.7
LGMphy	245.4 / 244.9	1.45 / 1.45	0.34 / 0.35	171 / 149	13.7 / 13.7	-0.4 / -0.4
RLS × 1.25	264.0 / 262.3	3.50 / 3.49	0.47 / 0.49	155 / 129	14.4 / 14.5	-0.5 / -0.4
LGMdust	262.2 / 256.9	3.48 / 3.47	0.46 / 0.49	152 / 124	14.4 / 14.5	-0.5 / -0.4
WNS × 0.5	265.1 / 261.7	3.98 / 3.99	0.51 / 0.52	141 / 114	12.7 / 12.7	-0.8 / -0.7
Acomb	222.5 / 214.9	1.45 / 1.45	0.48 / 0.39	148 / 116	13.7 / 13.7	-0.4 / -0.4
GLcomb	214.1 / 198.2	1.94 / 1.91	0.46 / 0.46	122 / 74	12.0 / 12.1	-0.4 / -0.4